Scientific Research Publishing

Computational Chemistry, 2025, 13(4), 69-101
https://www.scirp.org/journal/cc
ISSN Online: 2332-5984
ISSN Print: 2332-5968

Geometry Optimization, Quantum Chemical Analysis, Visual Study of Weak Interactions, and the Antifungal Activity Studies of Some Metal (II) Complexes of 1,4-Benzodioxane-6-Carbaldehyde Thiosemicarbazone by Molecular Docking

Roland B. Enongene[1], Gwendoline M. Toh-Boyo[1], Bridget N. Ndosiri[2], Emmanuel N. Nfor[1*], Offiong E. Ofiong[3], Hitler Louis[3,4]

[1]Department of Chemistry, Faculty of Science, University of Buea, Buea, Cameroon
[2]Department of Inorganic Chemistry, Faculty of Science, University of Yaoundé 1, Yaoundé, Cameroon
[3]Department of Pure and Applied Chemistry, Faculty of Physical Sciences, University of Calabar, Calabar, Nigeria
[4]Computational and Bio-Simulation Research Group, University of Calabar, Calabar, Nigeria
Email: *nfor.emmanuel@ubuea.cm

How to cite this paper: Enongene, R.B., Toh-Boyo, G.M., Ndosiri, B.N., Nfor, E.N., Ofiong, O.E. and Louis, H. (2025) Geometry Optimization, Quantum Chemical Analysis, Visual Study of Weak Interactions, and the Antifungal Activity Studies of Some Metal (II) Complexes of 1,4-Benzodioxane-6-Carbaldehyde Thiosemicarbazone by Molecular Docking. *Computational Chemistry*, **13**, 69-101.
https://doi.org/10.4236/cc.2025.134004

Received: July 13, 2025
Accepted: August 26, 2025
Published: August 29, 2025

Abstract

A new Schiff-base 1,4-benzodioxane-6-carboxaldehyde thiosemicarbazone (B1) and its Zn(II), Cu(II) Ni(II) and Mn(II) complexes (ZnB1, CuB1, NiB1 and MnB1) were synthesized and characterized. The FT-IR, ^{1}H-NMR and UV-Vis spectroscopy as well as elemental analysis, electrical conductivity measurement, thermal studies were all used to describe the structural features of the ligand and its metal (II) complexes. The metal complexes were found to exhibit octahedral geometry. Furthermore, computational studies using the DFT-B3LYP method are reported for the ligand B1 and its metal (II) complexes. The electronic property analysis revealed that, B1 serves as a strong electron donor due to its large positive energy gap (7.43Ev), indicating its propensity to participate as an electron donor in chemical reactions. A similar chemical behavior was observed with the CuB1 complex having an energy gap of 5.27 eV, suggesting its involvement, as an electron acceptor in the reaction, a bit weaker, compared to NiB1, with the highest energy gap of 7.23 eV. The ZnB1 and MnB1complexes also behaved as electron acceptors with energy gaps of 7.08 eV and 5.83 eV, respectively. The biological potential as lead compounds against *Candida albicans* infection was explored through molecular

docking analysis. The results revealed binding affinities of −8.2 kcal/mol, −8.1 kcal/mol, −8 kcal/mol, −7.9 kcal/mol, and −7.1 kcal/mol for NiB1, CuB1, ZnB1, MnB1 complexes, and B1 ligand, respectively. These results demonstrated that the protein receptor (5BTH) and the metal complexes exhibited strong binding capacity. Comparatively, the over-the-counter medication fluconazole (access code DB00196), which was used as a benchmark to validate the results, had a theoretical binding affinity of −8.2 kcal/mol, a value equivalent to that obtained for the metal complexes. Additionally, the mean binding affinities for the examined complexes NiB1, CuB1, ZnB1, and MnB1 were noticeably higher with values of −7.93 kcal/mol, −7.77 kcal/mol, −7.54 kcal/mol, and −6.48 kcal/mol, respectively. The nickel complex demonstrated appreciable biological activity and reactivity in its interactions with the 5BTH protein, comparable to the standard drug fluconazole.

Keywords

Synthesis, Candida Albicans, Molecular Docking, Metal Complexes, DFT

1. Introduction

Candidiasis has emerged as a serious healthcare problem due to its high incidence rate and the documented cases of drug resistance. Candidiasis caused by *Candida albicans* can present itself in diverse forms, encompassing thrush (oral candidiasis), vaginal infections, and systemic candidiasis, which is severe and potentially life-threatening [1]-[4]. In recent years, there has been a significant increase in the incidence of candidiasis, particularly among individuals with weak immune systems, such as those with HIV/AIDS, cancer patients undergoing chemotherapy, and organ transplant recipients who are prescribed immunosuppressive drugs [5] [6]. As with other fungal infections, the resistance of *Candida albicans* to drug is alarming. *Candida* species have the potential to develop resistance to frequently employed antifungal agents such as fluconazole, due to excessive or inappropriate use [7]-[9]. The emergence of resistance to chemotherapy poses significant challenges to treatment options [10] [11].

Benzodioxane, a heterocyclic compound composed of a benzene ring fused with a dioxane moiety and its derivatives have attracted significant research interest over the years, due to its diverse chemical reactivity and potential medicinal applications [12]. The 1,4-benzodioxane is an important scaffold in some biologically useful natural products including some lignins and neolignan, hence, has received significant attention in medicinal and pharmaceutical research [13]. In addition, 1,4-benzodioxane moiety is an important part of doxazosin, a drug used in the treatment of hypertension, and benign prostrate hyperplasia [14]-[16]. Furthermore, numerous studies have reported the pharmacological potential of 1,4-benzodioxane derivatives against a variety of diseases, including neurological disorders, cancer, inflammation and microbial infections [17]-[20].

The field of coordination chemistry has witnessed significant advances in recent years, driven by the quest for novel metal complexes with remarkable biological activities. Amongst these, thiosemicarbazone derivatives have gained considerable attention due to their diverse coordination abilities and potential medicinal applications [21]-[23]. In particular, metal (II) complexes derived from thiosemicarbazone ligands have exhibited promising antifungal properties, making them promising candidates for therapeutic intervention against fungal infections [24]-[28]. The present research work aims to explore the geometry optimization, quantum chemical analysis, visual study of weak interactions and the antifungal activities of some metal (II) complexes based on a thiosemicarbazone derivative. By employing molecular docking techniques, the study seeks to investigate the binding modes of these complexes with target fungal protein, shedding light on their potential as antifungal agents.

Thus we report herein the geometry optimization, quantum chemical analysis, weak interactions and antifungal activities studies of 1,4-benzodioxane-6-carboxaldehyde thiosemicarbazone (B1), (a derivative of two scaffolds 1,4-benzodioxane-6-carboxaldehyde and thiosemicarbazide) and its metal (II) complexes.

2. Materials and Methods

2.1. Materials and Physical Measurements

Thiosemicarbazide, 1,4-benzodioxane-6-carboxaldehyde, $NiCl_2.6H_2O$, $MnCl_2{\cdot}4H_2O$, $CuCl_2{\cdot}2H_2O$ and $ZnCl_2$ (Analar reagents) and solvents were obtained commercially from sigma Aldrich and used without further purification. The elemental analyses (e.g., carbon, hydrogen, nitrogen and oxygen) were collected at the State key Laboratory of Coordination Chemistry, Nanjing University, China, by a Perkin-Elmer CHNS/O 2400 series II Elemental Analyzer. The metal contents were determined gravimetrically by converting the compounds to its corresponding stable oxides. The chloride ions were gravimetrically determined using a standard method and the data reflect the high conformity with that theoretically proposed. The molar conductivities of freshly prepared 10^{-3} mol/cm^3 dimethylformamide (DMF) solutions were measured for the soluble complexes using Jenway 4010 conductivity meter. The infrared spectra, as KBr discs, were recorded on a Bruker FT-IR Spectrophotometer (4000 - 400 cm^{-1}) at State key Laboratory of Coordination Chemistry, Nanjing University, China. The electronic and ^{1}H-NMR (400 MHz) spectra were recorded on Varian Gemini Spectrophotometers at State key Laboratory of Coordination Chemistry, Nanjing University, China. The thermal studies were carried out on a Shimadzu thermo gravimetric analyzer at a heating rate of 10˚C min^{-1} under nitrogen till 800˚C in State key Laboratory of Coordination Chemistry, Nanjing University, China. The UV-vis spectrophotometer JASCO type V-550 was used to measure the diffused reflectance of the powder samples and to record the electronic spectra of 10^{-3} M in solid complexes, and DMF used as solvent.

2.2. Experimental Procedure

2.2.1. Syntheses of the Ligand

1) Synthesis of 1,4-benzodioxane-6-carboxaldehyde thiosemicarbazone (B1)

1,4-benzodioxane-6-carboxaldehyde (2.703 g, 0.019 mol) dissolved in 15 mL ethanol was, added to thiosemicarbazide (1.5 g, 0.0165 mol) in 15 mL of ethanolic solution with 3 drops of glacial acetic acid as catalyst. The resulting mixture was refluxed for 6 hours at a temperature of 80˚C. The product was left overnight to cool, collected by vacuum filtration and the precipitate washed several times with methanol and dried in a desiccator. A brown powder was obtained (Scheme 1). Yield = 80%, Mp: 209.4˚C, $C_{10}H_{11}N_3O_2S$, Elemental Analysis; *Found*: C, 50.60; H, 4.62; N, 17.69; O, 13.50, *Calculated*: C, 50.62; H, 4.67; N, 17.71; O, 13.49; IR (KBr) (υ, cm^{-1}): 3125.07 (NH), 3378.78 (NH_2), 1562.29 (C=N), 1439.29 (C=S), 1500.22 (C=C), 1062.57 (N-N); ^{1}H-NMR (400 MHz, DMSO-d_6 ppm) δ: 7.20 (m, 1H, NH), 7.10 (s, 2H, NH_2), 7.68 (s, 1H, CH), 4.30 (s, 4H, OCH_2-CH_2O), 9.12 (NH-CS).

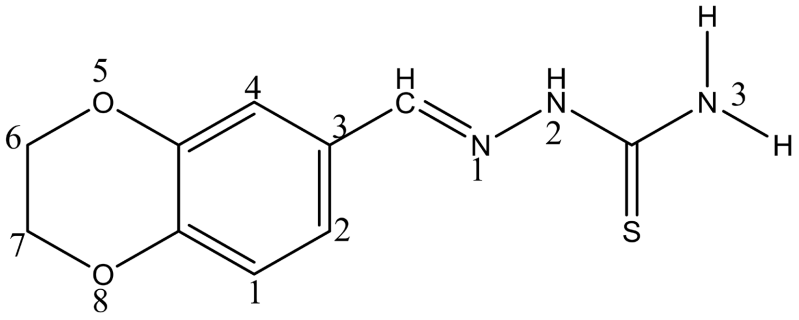

Scheme 1. Structure of 1,4-benzodioxane-6-carboxaldehydethiosemicarbazone (B1).

2.1.2. Synthesis of the Metal Complexes

1) Synthesis of zinc (II) complex

Zinc(II)chloride (0.2 g, 1.0 mmol) was added to 1,4-benzodioxane-6-carboxaldehyde thiosemicarbazone (0.704 g, 2.0 mmol) in a 25 mL ethanolic solution. The resulting mixture was refluxed for 4 hours at a temperature of 80˚C with continuous stirring using magnetic stirrer. The greenish solution obtained was allowed to cool, the precipitate removed by filtration, washed several times with ethanol and stored in desiccator. Mp: 216.8˚C, $C_{20}H_{22}Cl_2N_6O_4S_2Zn$, Elemental Analysis; *Found*: C, 39.36; H, 13.80; N, 13.73; O, 10.46, *Calculated*; C, 39.33; H, 3.63; N, 13.76; O, 10.48; IR (KBr) (υ, cm^{-1}): 2960.07 (NH), 3433.60 (NH_2), 1624.38 (C=N), 1460.29 (C=S), 1562.29 (C=C), 1010.27 (N-N), 625.07 (M-N), 507.35 (M-S), 460.45 (M-Cl); ^{1}H-NMR (400 MHz, DMSO-d_6 ppm) δ: 7.02 (m, 1H, NH), 7.23 (s, 2H, NH_2), 7.62 (s, 1H, CH), 4.63 (s, 4H, OCH_2-CH_2O), 9.84 (NH-CS).

2) Synthesis of copper (II) complex

Copper (II) chloride dihydrate (0.2 g, 1.0 mmol) was added to 1, 4-benzodioxane-6-carboxaldehyde thiosemicarbazone (0.704 g, 2.0 mmol) in a 25 mL ethanolic solution. The resulting mixture was refluxed for 4 hours at a temperature of 80˚C with

continuous stirring using magnetic stirrer. The greenish solution obtained was allowed overnight to cool, the precipitate removed by filtration, washed with ethanol and stored in desiccator. *Yield*: 82%, Mp: 218.6˚C, $C_{20}H_{22}Cl_2N_6O_4S_2Cu$, Elemental Analysis; *Found*: C, 39.46; H, 3.67; N, 13.82; O, 10.55, *Calculated*: C, 39.44; H, 3.64; N, 13.80; O, 10.51; IR (KBr) (υ, cm^{-1}): 3141.34 (NH), 3420.51 (NH_2), 1602.41 (C=N), 1430.11 (C=S), 1503.16 (C=C), 1061.16 (N-N), 611.86 (M-N), 533.79 (M-S), 460.56 (M-Cl); ^{1}H-NMR (400 MHz, DMSO-d_6 ppm) δ: 6.89 - 7.48 (m, 1H, NH), 8.00 (s, 2H, NH_2), 8.63 (s, 1H, CH), 4.28 (s, 4H, OCH_2-CH_2O), 11.78 (NH-CS).

3) Synthesis of nickel (II) complex

Nickel (II) chloride hexahydrate (0.2 g, 1.0 mmol) was added to 1, 4-benzodioxane-6-carboxaldehyde thiosemicarbazone (0.396 g, 2.0 mmol) in a 25 mL ethanolic solution. The resulting mixture was refluxed for 4 hours at a temperature of 80˚C with continuous stirring using magnetic stirrer. The colourless solution obtained was allowed overnight to cool, the precipitate removed by filtration, washed with ethanol and stored in desiccator. *Yield*: 75%, Mp: 214.6˚C, $C_{20}H_{22}Cl_2N_6O_4S_2Ni$, Elemental Analysis; *Found*: C, 39.78; H, 3.66; N, 13.87; O, 10.73, *Calculated*: C, 39.76; H, 3.67; N, 13.91; O, 10.59; IR (KBr) (υ, cm^{-1}): 3155.14 (NH), 3430.29 (NH_2), 1563.99 (C=N), 1455.70 (C=S), 1539.68 (C=C), 1060.90 (N-N), 624.28 (M-N), 541.04 (M-S), 450.13 (M-Cl); ^{1}H-NMR (400 MHz, DMSO-d_6 ppm) δ: 6.86 - 7.41 (m, 1H, NH), 7.92 (s, 2H, NH_2), 8.09 (s, 1H, CH), 4.28 (s, 4H, OCH_2-CH_2O), 11.30 (NH-CS).

4) Synthesis of manganese (II) complex

Manganese (II) chloride tetrahydrate (0.2 g, 1.0 mmol) was added to 1,4-benzodioxane-6-carboxaldehyde thiosemicarbazone (0.756 g, 2.0 mmol) in a 25 mL ethanolic solution. The resulting mixture was refluxed for 4 hours at a temperature of 80˚C with continuous stirring using magnetic stirrer. The colourless solution obtained was allowed overnight to cool, the precipitate removed by filtration, washed with ethanol and stored in desiccator. *Yield*: 85%, Mp: 221.8˚C, $C_{20}H_{22}Cl_2N_6O_4S_2Mn$, Elemental Analysis; *Found*: C, 40.03; H, 3.69; N, 14.07; O, 10.73, *Calculated*: C, 40.02; H, 3.67; N, 14.05; O, 10.66; IR (KBr) (υ, cm^{-1}): 3151.37 (NH), 3406.94 (NH_2), 1584.96 (C=N), 1456.20 (C=S), 1539.73 (C=C), 1057.22 (N-N), 577.58 (M-N), 541.04 (M-S), 450.13 (M-Cl); ^{1}H-NMR (400 MHz, DMSO-d_6 ppm) δ: 6.86 - 7.42 (m, 1H, NH), 7.90 (s, 2H, NH_2), 8.09 (s, 1H, CH),4.25 (s, 4H, OCH_2-CH_2O), 11.30 (NH-CS).

2.3. Computational Studies

Theoretical calculations were conducted using Density Functional Theory (DFT) within the WB97XD functional, employing the 6-311++G (d,p) basis set. The optimization of the ligand and metal (II) complexes and additional calculations based on DFT were performed [29]. To account for dispersion interactions, the empirical dispersion def2tzvp was integrated [30]. To verify the accuracy of optimized results as local energy minima, frequency optimizations were conducted, ensuring the absence of imaginary frequencies. The optimization processes were

executed utilizing the Gaussian 16 software. For determining atomic charges, orbital configurations, and orbital contributions to charge transfer and stabilization energies, a computational assessment was carried out using Natural Bond Orbital (NBO) analysis with NBO version 3.1, integrated into Gaussian 16 software [31]. The electronic characteristics of the ligand and its metal (II) complexes, such as the Highest Occupied Molecular Orbital (HOMO), Lowest Unoccupied Molecular Orbital (LUMO), and Density of States (DOS), were visualized using Chemcraft and Origin software [32]. An analysis of noncovalent interactions (NCI) was undertaken to comprehend the interaction nature within the studied complexes, employing Multiwfn. Moreover, the interaction strength was confirmed by examining key topological parameters, including electron density (p), Laplacian ($\nabla 2\rho$), and total electron energy density (H(r)), localized at bond critical points (BCP). These BCPs were obtained through Quantum Theory of Atoms in Molecules (QTAIM) analysis.

2.4. Molecular Docking Studies

Molecular docking with a pivotal role in the domain of structure-based drug design, was employed to evaluate the interaction of the investigated compounds with the virulent proteins of *Candida albicans Rai1*. The selected protein structures, obtained from the Protein Data Bank (https://www.rcsb.org/) with PDB files (5BTH), were prepared using Discovery Studio.

The protein 5BTH was chosen as target receptor because it represents the N-terminal region of the Rai1 protein, an intriguing molecule found in *Saccharomyces cerevisiae*, which is a common yeast species. *Rai1*, which stands for "regulator of axon regeneration 1", is a multifunctional enzyme with roles spanning from RNA metabolism, processing, and quality control [33]. It is associated with a variety of cellular functions that influence gene expression and RNA surveillance. In the context of *Saccharomyces cerevisiae*, *Rai1* has been linked to the regulation of RNA decay and surveillance pathways, playing a crucial role in maintaining the integrity and stability of the cellular RNA pool [34]. It participates in the removal of aberrant or misprocessed RNAs, contributing to the overall quality control mechanisms of the cell. Investigating this region can shed light on the molecular mechanisms underlying RNA processing, decay, and surveillance in yeast cells. Such insights have broader implications, as they may provide valuable clues about conserved RNA quality control mechanisms in other organisms, including higher eukaryotes. The utilization of this protein structure (5BTH) in molecular docking studies suggests an interest in understanding how small molecules or ligands interact with the *Rai1* protein. These interactions could potentially modulate *Rai1's* RNA-related functions, offering potential avenues for therapeutic intervention or further elucidating its cellular roles.

2.4.1. Protein and Ligand Preparation

The preparation of the protein was carried out utilizing Biovia Discovery Studio 21 [35]. The initial step involved removing water molecules and native ligands

from the protein. Following this, polar hydrogen atoms were introduced to improve binding compatibility. Subsequently, the compounds and target proteins were input into the PyRx virtual screening program [36].

2.4.2. Docking Process

In the docking process, the target proteins were converted into a macromolecular format, and the docking parameters were configured. The grid box was precisely positioned at the active site of the protein, aligned with the crystal structures. The grid box settings were adjusted as follows: center x = −22.9760, center y = 49.3510, and center y = 31.2970 for the protein. The assessment of docking outcomes revolved around binding affinity. The conformational arrangements exhibiting specific interactions with active-site residues were comprehensively scrutinized using Discovery Studio and PyMOL. Emphasizing on the result credibility, a meticulous examination was conducted to elucidate the interactions formed between the compounds and the target proteins. The discovery Studio played a pivotal role in delving into interaction intricacies, encompassing hydrogen bonds, halogen bonds, alkyl interactions, and van der Waals forces. Notably, hydrogen bonds, a prevailing force in biological systems, assumed a significant role [37]. The stability of protein-ligand interactions was evaluated through the hydrogen bonds lengths; shorter bond lengths indicated robust connections between the protein and the ligand [38].

3. Results and Discussion

3.1. Physiochemical Properties

The elemental analyses for C, H, N and O revealed that the calculated values for the ligand L are in agreement with the experimental values, thus confirming the proposed molecular formula $C_{10}H_{11}N_3O_2S$ for the ligand. The agreement between the calculated and experimental elemental analyses values for the metal complexes revealed a 1:2 (metal-ligand) stoichiometry, thus confirming their suggested formulae. These results further confirmed the high purity of the Schiff base and its metal (II) complexes which were very soluble in DMSO and less soluble in methanol. The ligand B1 melted at the temperature of 209.4˚C while its zinc, copper, nickel and manganese complexes melted with decomposition at the temperatures of 216.8˚C, 218.9˚C, 214.6˚C and 221.3˚C respectively.

3.2. Conductivity Measurements

The molar conductivity studies of the prepared compounds were evaluated to ascertain their electrolytic nature. They were first dissolved in DMF at room temperature at a concentration of 1.0×10^{-3} M. The molar conductivity of ZnB1, CuB1, NiB1 and MnB1 were found to be 12.22, 17.33, 16.79 and 18.72 $\Omega^{-1}\cdot cm^2\cdot mol^{-1}$ respectively, which are low molar conductance values and could be attributed to their non-electrolytic nature [39]. The molar conductance values provides useful information on the metal to ligand stoichiometry. It has been

observed that metal complexes with 1:2 metal to ligand stoichiometry have lower molar conductance values as compared to those with 1:1 metal-ligand stoichiometry [40].

3.3. Infrared Spectroscopic Analysis

The infrared spectra of the ligand B1 and its metal (II) complexes were recorded within the 4000 cm^{-1} - 400 cm^{-1} region. The spectra can be seen in **Figures S1-S5**. The infrared spectral bands, most useful for determining the coordination mode of the ligand (B1) were the v(C=N), v(N-N) and v(C=S) vibrations. The v(C=N) band in the free ligand is 1562 cm^{-1}, while in the complexes ZnB1, CuB1, NiB1 and MnB1, the band experiences a shift to 1624 cm^{-1}, 1602.48, 1563.99 and 1584.96 cm^{-1} respectively, as compared to that of the ligand, indicating a clearly the coordination of the metal ions *via* the imine nitrogen atom [41] [42]. In the ligand B1, a band at 1439 cm^{-1} is assigned to v(C=S) whereas in its complexes, the band shifted to 1460 cm^{-1} in ZnB1, 1430.11 cm^{-1} in CuB1, 1455.7 cm^{-1} NiB1 and to 1356 cm^{-1} in MnB1 indicating the coordination of thioamide sulphur atom to the metal ions [43]. The increase in the vibrational frequency of v(N-N) band of B1 in the spectra of complexes which is attributed to the increase in bond strength, further confirms the coordination *via* the imine nitrogen [44]. Bands in the region 533 - 635 cm^{-1} and 448 - 577 cm^{-1} are probably due to M-N and M-S bonds respectively. The M-Cl vibrational bands fall in the region 416 - 490 cm^{-1} [44] [45].

3.4. Proton NMR Spectra Studies

The ^{1}H-NMR spectroscopic data for B1 and its complexes in DMSO-d_6 are reported in the experimental section, while their spectrum are in **Figures S6-S10**. These data are in close agreement with previously reported work [46]. The spectrum of the free B1 (**Figure 1** for numbering scheme) exhibited the following signals δ 7.20 for (1H, NH), δ 7.10 for (2H, NH_2), δ 7.68 (1H, CH) and δ 4.30 ppm for –OCH_2-CH_2O-. The band at δ 912 ppm in B1 is attributed to NHCS.

In the ^{1}H-NMR spectrum of the ZnB1 complex, it showed a signal at δ 7.02 attributed to the azomethine proton (HC=N), an upfield shift compared to that of the free ligand B1. The signal at δ 9.84 was attributed to the thioamide proton (NHC=S). While that at δ 7.23 assigned to the amine protons (2H, NH_2) [46]-[48].

The ^{1}H-NMR spectrum of CuB1 complex showed signals at δ 6.89 - 7.48, δ 11.28 and δ 8.00ppm attributed to the (HC=N), (NHC=S) and (2H, NH_2) protons respectively [48].

The ^{1}H-NMR spectrum of the NiB1 complex, exhibited bands associated with the azomethine proton (HC=N) at δ 6.86 - 7.41 ppm, 11.30 for the thioamide proton (NHC=S) and δ 7.92 for the amine nitrogen (2H, NH_2) respectively. On the other hand, the MnB1 complex exhibited signals at δ 6.86 - 7.42 ppm for the azomethine proton (HC=N), δ 11.30 ppm for the thioamide (NHC=S) protons and δ 7.90 ppm for the amine (2H, NH_2) protons. Therefore based on the proton NMR

assignments of the complexes, it is evident that the metal ions coordinated to the ligand B1, through the azomethine nitrogen and thioamide sulphur atoms.

3.5. Electronic Spectra Studies

The electronic absorption spectroscopic technique was used in this investigation to ascertain the coordination geometry and estimates the intra-ligand, ligand–metal, and d–d electronic transitions of the prepared compounds. The UV-visible spectra of the metal complexes are presented in **Figure 1**. The spectral data of BI exhibited absorption bands at 270, 296, 316, 345, and 410 nm with the higher energy bands (345, 410 nm) assigned to $\pi\rightarrow\pi^*$ transitions within aromatic rings [49] [50], and the lower energy bands (270 - 316 nm) assigned to $n\rightarrow\pi^*$ transitions within C=O and C=N groups respectively [51]-[53]. In the metal complexes, the $\pi\rightarrow\pi^*$ and $n\rightarrow\pi^*$ transitions changed thus revealing the coordination between the metal ions and the B1 ligand. The ligand-metal charge transfer (LMCT) transitions were observed in the range of 415 - 451 nm [54]. Generally the metal complexes exhibited absorption bands in the range 580 - 660 nm, attributed to d-d transitions [55].

The zinc complex showed absorption bands at 288, 318 and 415 nm (**Figure 1**) that could be attributed to the $\pi\rightarrow\pi^*$, $n\rightarrow\pi^*$and charge transfer transitions respectively. The electronic spectrum of the ZnB1 complex did not however include any specific evidence of the stereochemistry but an octahedral geometry was proposed based on the analytical, thermal, infrared and proton NMR spectral data available.

For the CuB1 complex, it showed a broad band in the visible region at 580 nm (**Figure 1**). This band is assigned to $^2E_g\rightarrow{}^2T_{2g}$ transition in the distorted octahedral around the copper complex [56] [57]. However, the low symmetry of the environment around the d^9 copper (II) ion and the Jahn-Teller distortion, made the complete interpretation of the electronic spectra of CuB1 complex a little complicated [58].

The spectra of octahedral Ni(II) complexes are always associated with three bands assigned to $^3A_{1g}(F)\rightarrow{}^3T_{2g}(F)$, $^3A_{2g}(F)\rightarrow{}^3T_{1g}(F)$ and $^3A_{2g}(F)\rightarrow{}^3T_{1g}(P)$ transitions. The first transition $^3A_{1g}(F)\rightarrow{}^3T_{2g}(F)$, was not observed as it lies in the near infrared which was out of range of the machine used. The spectrum of the NiB1 complex **Figure 1** revealed a broad band at 585 nm attributed to the $^3A_{2g}(F)\rightarrow{}^3T_{1g}(F)$ transition that favors octahedral geometry.

For the MnB1 complex, it revealed that, the complex has an octahedral geometry. The electronic transition which can be explained using the Tanabe-Sugano diagram revealed that octahedral manganese (II) complexes spectra usually contain three bands [59]. The first band which is ascribed to $^6A_{1g}(F)\rightarrow{}^4T_{1g}(^4G)$ transition, was not detected due to the fact that, it lies in the near infrared region and out of the range of instrument used. In the current work, only one broad band was observed in the visible region (660 nm) which may be due may be due to the $^6A_{1g}\rightarrow{}^4E_g(^4D)$ transition in an octahedral geometry.

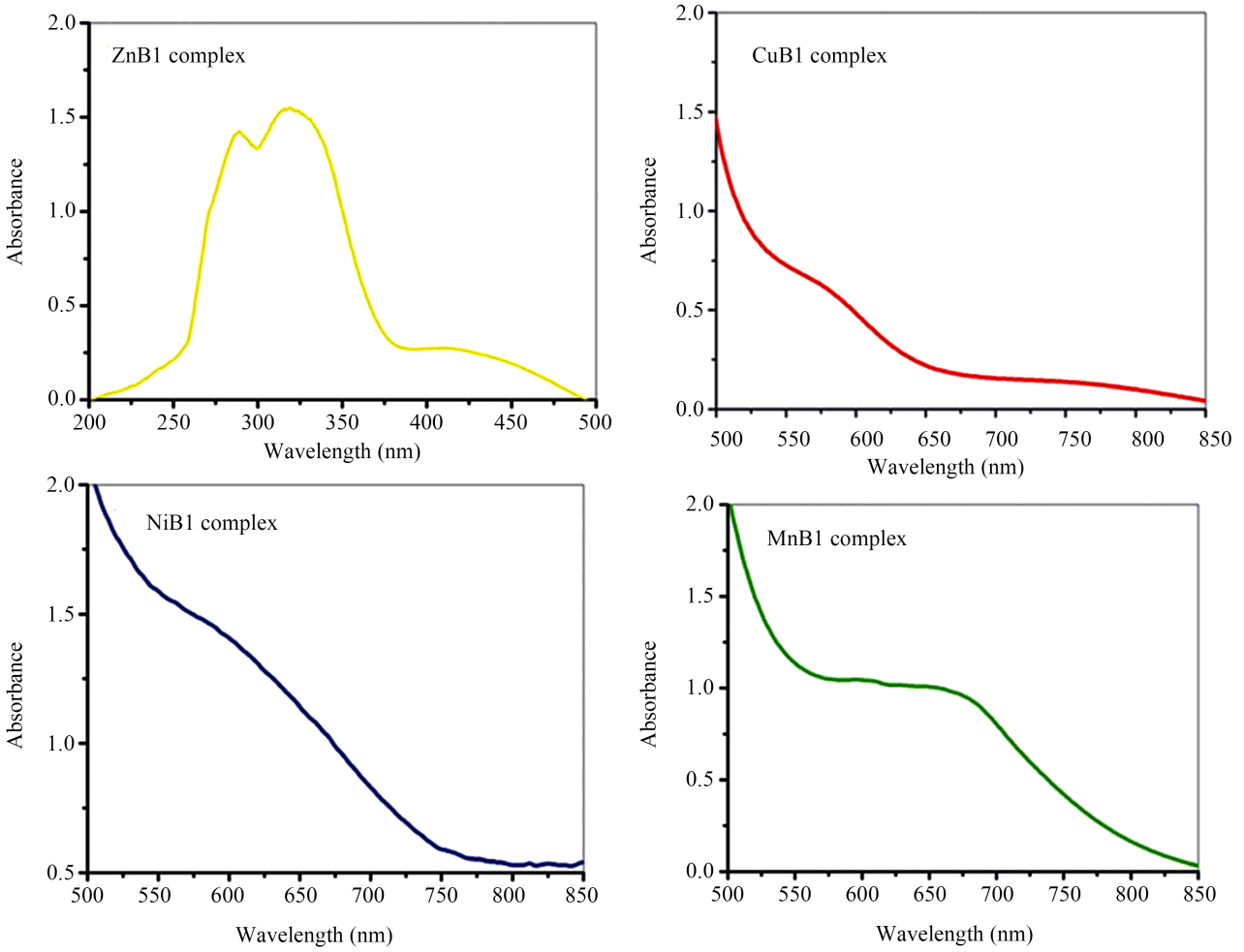

Figure 1. UV-Vis spectra of transition the metal (II) complexes in DMF solvent.

3.6. Thermal Studies

The TGA analysis of the synthesized compounds offers valuable details on the stability of the complexes. The thermal degradation steps of the ligand and its metal (II) complexes are presented in **Table 1**. The TGA curve of the ligand B1, decomposed in two stages over a temperature range of 30˚C - 800˚C. The first step occurred in the temperature range of 120˚C - 250˚C with a percentage weight loss 16.02% attributed to the loss of methylamine (CH_3NH_2). The second step of degradation falls in the temperature range of 251˚C - 755˚C with weight loss of 64.0% which is due to loss of an aromatic nitrogenous group $C_7H_6N_2O$.

The thermal decomposition of ZnB1 complex took place in three steps. The first step occurred in the temperature range of 50˚C - 260˚C with weight loss of 8.27% corresponding to the loss of two water molecules and EtOH. The second step of decomposition which occurred in the temperature range of 260˚C - 395˚C with weight loss of 45.27% has been assigned to the loss of chlorinated phenyl plus SO_2NH including diazine. The third decomposition step which occurred in the temperature change of 395˚C - 770˚C with percentage weight loss of 18.54%

corresponds to the loss of the remaining C/N fragment plus HCl.

The CuB1 complex proceeded with three degradation steps, with the first step in the temperature range of 30˚C - 230˚C having weight loss of 8.27% assigned to the loss of 1.4 equivalent of HCl.

The second step was in the temperature range of 231˚C - 410˚C, with percentage weight loss of 45.95% due to the loss of $C_{10}H_{11}ClN_3O_2S$. The third decomposition step occurred within the temperature range of 411˚C - 620˚C with 29.6% weight loss attributed to the loss of remaining C/N/O fragment.

The thermal decomposition of NiB1 complex proceeds with three degradation steps. The first step in the temperature range of 50.45˚C - 199˚C experienced a mass loss of 5.30% assigned to the elimination of CH_3CN. The second step was in the temperature range of 200˚C - 361˚C with weight loss of 65.13% attributed to the loss of Chlorinated-phenyl ring and SO_2NH. The third step decomposition of nickel was within the temperature range of 360˚C - 670˚C having weight loss of 33.20% that has been assigned to the elimination of HCl, SO_2 and the residual aromatic fragment.

Finally the manganese complex MnB1 underwent three step thermal decomposition. The first step decomposition took place in the temperature range of 30.7˚C - 180˚C with weight loss of 6.61% attributed to the loss of CH_3CN, $2H_2O$ and Ethanol. On the other hand, the second step decomposition was within the temperature range of 180˚C - 290˚C with weight loss of 68.10% attributed to the elimination of Cl-C_4H_4, SO_2NH and diazine. Furthermore, the third step of decomposition was in the temperature range of 291˚C - 440˚C with the weight loss of 25.16% attributed to the loss of HCl, SO_2 and residual aromatic fragment.

Table 1. Thermal analysis of the ligand and its metal (II) complexes.

Compound	Temperature Range ˚C	%Total loss in weight Found (Calc.)	Fragment lost
B1	120 - 250	16.02 (16.02)	CH_2NH_2
	251 - 755	64.00 (64.00)	$C_7H_6N_2O$
ZnB1	50 - 260	8.27 (8.27)	H_2O + EtOH
	260 - 395	45.27 (45.32)	C_6H_6Cl
	395 - 770	18.54 (18.56)	Remaining N/O/S fragment
CuB1	30.9 - 230	8.27 (8.29)	1.4 equv. HCl
	230 - 410	45.95 (45.91)	$C_{10}H_{11}ClN_3O_2S$
	410 - 620	29.6 (29.60)	Remaining N/O/S fragment
NiB1	50.45 - 199	5.30 (5.30)	CH_3CN
	200 - 360	65.13 (65.13)	Cl-phenyl ring + SO_2NH
	360 - 670	33.20 (33.20)	HCl + SO_2 + Residual aromatic fragment
MnB1	30.7 - 180	6.61 (6.61)	CH_3CN +$2H_2O$, Ethanol
	180 - 290	68.10 (68.10)	Cl-C_4H_4 +SO_2NH+ diazine HCl+SO_2 + Residual
	290 - 440	25.16 (25.16)	Aromatic fragment

3.7. Geometry Optimization

The structures B1, CuB1, MnB1, NiB1 and ZnB1 were optimized using the DFT method and the WB97XD functional. The geometric parameters analyzed include bond length and bond angles. The optimized geometries of the proposed structures of ZnB1, CuB1, NiB1 and MnB1 complexes are presented in Figure 2, while the bond lengths and bond angles of the optimized structures of the ligand B1 and its metal (II) complexes are presented in Table 2.

For B1, the C_{23}-S_{27}, N_{20}-N_{21}, and N_{20}-C_{18} bond lengths are 1.6643, 1.3617 and 1.2802 Å respectively. These values are in agreement with previously reported results with similar ligands [60]. The N_{20}-N_{21} bond length of all the metal complexes are within the 1.3560 - 1.4002 Å range, though with slight deviation from that of the ligand B1, further confirming coordination of the imine nitrogen. The metal-nitrogen (M-N) bond lengths of all the complexes are in the range of 1.9434 Å - 3.4067 Å, the metal-sulphur bond lengths of the complexes falling within the range of 2.1550 - 2.3422 Å. These observed bond lengths are all in agreement with previous works [60]. In the optimized structure of B1, the N_{21}-C_{23}-S_{27} bond angle is 119.74 Å, while the Cl_{54}-Cu_{57}-S_{55}, Cl_{54}-Cu_{57}-N_{21} in CuB1 are 87.40 and 41.62 Å respectively. In MnB1, The Cl_{54}-Mn_{57}-S_{55} and Cl_{54}-Mn_{57}-N_{21} are 92.38 and 103.70 Å respectively. On the other hand, in the NiB1 complex, the Cl_{54}-Ni_{57}-S_{55} and Cl_{54}-Ni_{57}-N_{21} bond angles are 88.83 and 119.50 Å. Similarly for the ZnB1 complex, the Cl_{54}-Zn_{57}-S_{55} and Cl_{54}-Zn_{57}-N_{21} bond angles are 98.20 and 83.28 Å respectively.

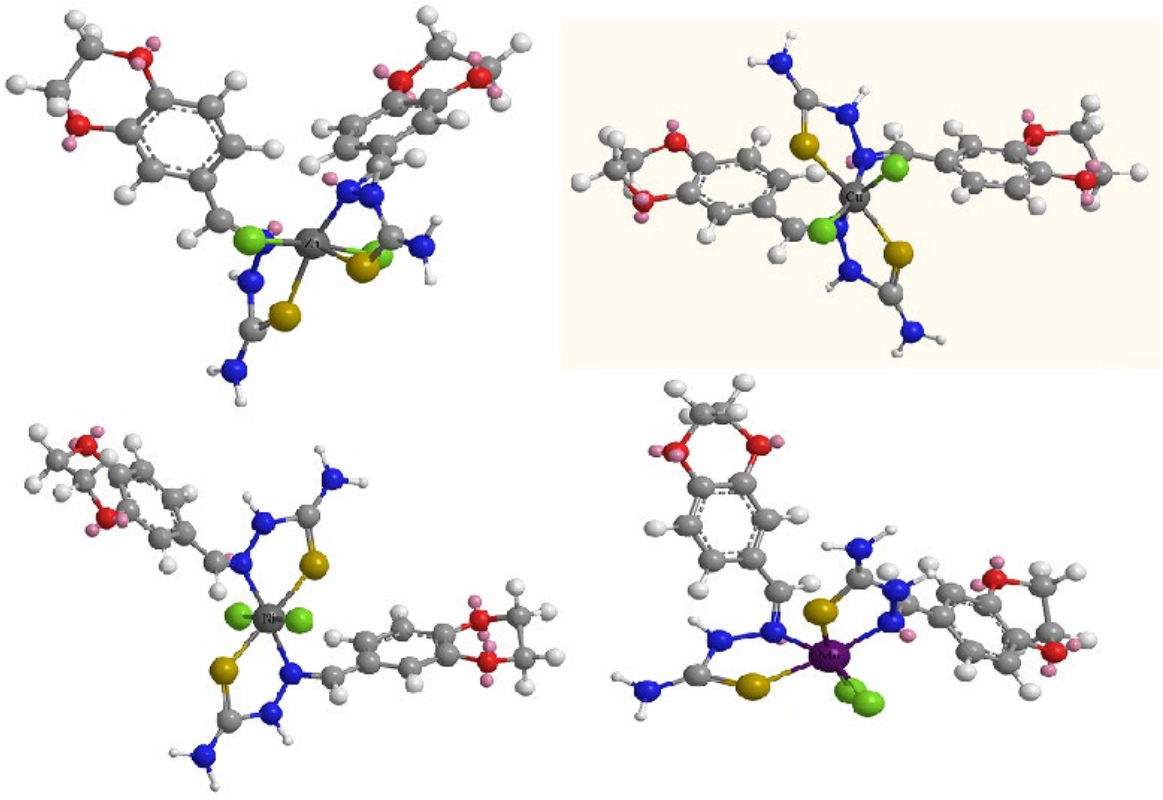

Figure 2. Optimized geometries of the proposed structures of ZnB1, CuB1, NiB1 and MnB1 complexes.

Table 2. Geometry bond distance of the ligand and it metal complex derivatives.

System	Bonds	Bond length (Å)	Atoms	Bond angle (˚)
	C23-S27	1.6643	N21-C23-S27	119.74
B1	N20-N21	1.3617	C18-N20-N21	120.96
	N20-C18	1.2802	N20-C18-H19	122.50
	N20-N21	1.4002	N20-N21-Cu57	86.70
	Cu57-N47	1.9434	Cu57-N47-H48	87.79
CuB1	Cu57-S55	2.1102	Cl54-Cu57-S55	87.40
	Cu57-Cl53	2.1510	Cl54-Cu57-Cl53	174.09
	Cu57-Cl54	2.1601	Cl54-Cu57-N21	41.62
	N20-N21	1.3669	N20-N21-Mn57	133.84
	Mn57-N47	2.7656	Mn57-N47-H48	72.57
MnB1	Mn57-S55	2.5118	Cl54-Mn57-S55	92.38
	Mn57-Cl53	2.3587	Cl54-Mn57-Cl53	178.28
	Mn57-Cl54	2.3099	Cl54-Mn57-N21	103.75
	N20-N21	1.3560	N20-N21-Ni57	147.57
	Ni57-N47	3.4067	Ni57-N47-H48	49.02
NiB1	Ni57-S55	2.2992	Cl54-Ni57-S55	88.83
	Ni57-Cl53	2.2482	Cl54-Ni57-Cl53	162.75
	Ni57-Cl54	2.2090	Cl54-Ni57-N21	119.50
	N20-N21	1.3587	N20-N21-Zn57	118.82
	Zn57-N47	3.1984	Zn57-N47-H48	57.46
ZnB1	Zn57-S55	2.5232	Cl54-Zn57-S55	98.20
	Zn57-Cl53	2.3422	Cl54-Zn57-Cl53	111.60
	Zn57-Cl54	2.2814	Cl54-Zn57-N21	83.28

3.7.1. Electronic Properties

1) HOMO-LUMO & Quantum descriptors studies

The HOMO and LUMO values of molecules play crucial roles in determining their electron-donating and electron-accepting abilities. These values are very essential in providing vital information on some properties of the molecules, including their photochemical reactions, luminescence, UV-vis spectroscopy, quantum chemistry, and pharmaceutical applications. Moreover, understanding the HOMO and LUMO values can shed light on the biological mechanisms and interactions of the molecules within living systems [61] [62]. The HOMO-LUMO and quantum descriptors of the studied compounds are presented in **Table 3**, while the isosurface of the HOMO and LUMO orbitals of the complexes are depicted in **Figure 3**. In **Table 3**, it is observed that B1 has large positive energy gap (7.43 ev) indicating that it is a strong electron donor. This implies that it is a soft molecule and likely to be involved in chemical reaction, where it serves as an electron donor. CuB1 had an energy gap of 5.27 eV, also likely to be involved in chemical reactions where it accepts electrons and a weaker electron acceptor compared to NiB1 with

an energy gap of 7.23 eV which is the highest. ZnB1 and MnB1 are also electron acceptors with the following energy gap of 7.08 eV and 5.83 eV respectively. Other analyses of the studied molecule's chemical reactivity parameters, such as chemical softness (S), chemical potential (μ), electrophilicity index (ω), and chemical hardness (η), were also carried out with the assistance of the energies from the HOMO-LUMO, using Equations (2)-(6). The result of the calculated parameters of the electronic properties are given in Table 3.

$$E_{gap} = E_{HOMO} - E_{LUMO} \tag{1}$$

$$\mu \approx \frac{\left(\varepsilon_{LUMO} + \varepsilon_{HOMO}\right)}{2}\left(\text{Chemical potential}\right) \tag{2}$$

$$\eta = \frac{E_{HOMO} - E_{LUMO}}{2}\left(\text{Chemical hardness}\right) \tag{3}$$

$$\omega = \frac{\mu^2}{2\eta}\left(\text{Electrophilicity index}\right) \tag{4}$$

$$\sigma = \frac{1}{\eta}\left(\text{chemical softness}\right) \tag{5}$$

$$\chi = -\mu = \frac{IP + EA}{2}\left(\text{electronegativity}\right) \tag{6}$$

The electrophilicity index which is a measure of the tendency of an atom or molecule to attract electrons, was as follows for the prepared compounds: B1 = 1.95 eV, CuB1 = 1.44 eV, NiB1 = −1.80 eV, ZnB = 2.34 eV, MnB1 = 1.84 eV. The values showed that, ZnB1 with the electrophilicity index of 2.34 eV has a strong ability to act as an electrophile. As for the chemical potential values of the compounds, there are as follows; B1 = −3.81 eV, CuB1 = 2.87 eV, NiB1 = −3.61 eV, ZnB1 = 4.07 eV, and MnB1 = 3.28 eV. These chemical values indicate that B1 and NiB1 have a high chemical potential by virtue of their inclination to interact or react with their environment. Furthermore a lower or more negative chemical potential value generally indicates higher reactivity as compared to a higher or more positive value. CuB1, ZnB1, and MnB1 all have positive values, which point to the compounds' relative stability and low likelihood of undergoing reactions or exchanges. The chemical hardness values show that B1 requires 3.72 eV of energy to either add or remove an electron, while CuB1, NiB1, ZnB1 and MnB1 have negative values; −2.64 eV, −3.62 eV, −3.54 eV and −2.94 eV respectively, indicating that they are more reactive and can readily undergo chemical conformations.

Table 3. The HOMO, LUMO band gap energy and quantum descriptor of the ligand and its metal complexes.

Compound	$E_{HOMO/ev}$	$E_{LUMO/ev}$	E_g (eV)	μ (eV)	η (eV)	ω (eV)	χ (eV)	σ
B1	7.529	0.099	7.43	−3.81	3.72	1.95	3.81	0.27
CuB1	−5.503	− 0.233	5.27	2.87	−2.64	1.44	−2.87	−0.38
NiB1	−7.735	−0.507	7.23	−3.61	−3.62	−1.80	3.61	−0.28
ZnB1	−7.605	−0.528	7.08	4.07	−3.54	2.34	−3.54	−0.28
MnB1	−6.194	−0.3610	5.83	3.28	−2.92	1.84	−2.92	−0.34

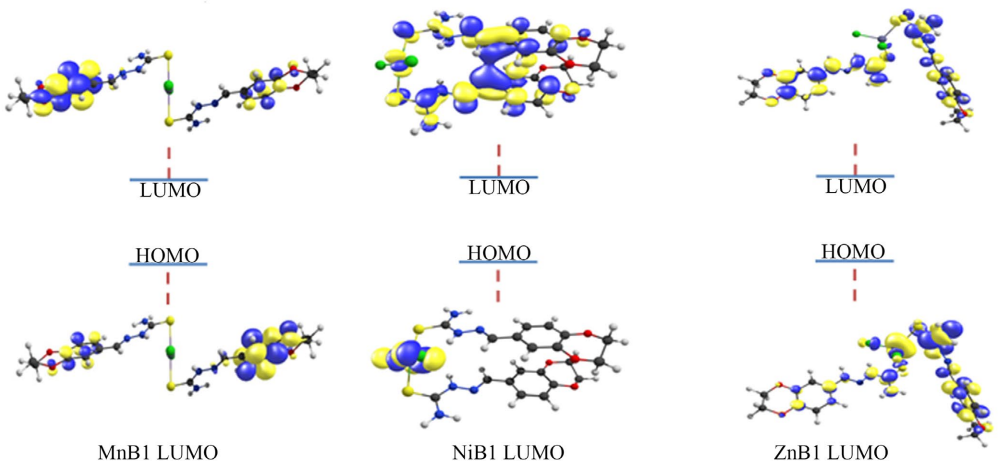

Figure 3. The iso-surface of the HOMO-LUMO orbital of the complexes.

2) Natural Bond Orbital (NBO) studies

NBO analysis is an important procedure to indicate the most possible natural Lewis structure picture of orbitals [63]. The compounds were subjected to NBO analysis to show the intra and inter molecular interaction between the orbitals, being a measure of hyperconjugation or intramolecular delocalization. Table 4 depicts the second order perturbation theory analysis of fock matrix on NBO basis for B1, CuB1, NiB1, ZnB1, and MnB1. In NiB1 significant interaction was very much evident due to the interaction of the donor, with the acceptor orbital π* (C29-C33)→π* (C34-C35) with resonance energy of 457.71 kcal/mol, ZnB1 – π* (C2-C3)→π* (C6-C9) with resonance energy of 369.37 kcal/mol, B1 – π* (C2-C3)→π* (C6-C9) having an energy of 357.95 kcal/mol, and CuB1 – π* (C2-C3)→π* (C6-C9) with 180.51 kcal/mol as its resonance energy. This shows that NiB1 exhibits the most significant hyperconjugative interaction with the highest resonance energy, indicating strong stabilization due to the interaction between donor and acceptor orbitals. ZnB1 and B1 share the same pair of donor and acceptor orbitals, suggesting similar electronic characteristics. The CuB1 complex showed a relatively weaker hyperconjugative interaction compared to the other compounds.

Table 4. Second-order perturbation theory analysis of Fock matrix on NBO basis of the ligand and its metal (II) complexes.

Compound	Donor orbital	Occ.	Acceptor orbital	Occupancy	$E_{(2)}$ kcal/mol	$E_{(j)}$-$E_{(i)}$ a.u.	$F_{(i,j)}$ a.u.
B1	π* C2-C3	0.40821	π* C6-C9	0.39046	357.95	0.01	0.101
	π* C2-C3	0.40821	π* C7-C8	0.31940	190.97	0.02	0.099
	πC2-C3	1.64036	π* C6-C9	0.39046	35.18	0.41	0.108
	πC2-C3	1.64036	π* C7-C8	0.31940	32.23	0.42	0.105
CuB1	π* C2-C3	0.20785	π* C6-C9	0.19863	180.51	0.01	0.102
	π* C2-C3	0.20785	π* C7-C8	0.16699	110.69	0.02	0.101
	π* C18-N20	0.12926	π* C6-C9	0.19863	35.27	0.03	0.071
	LP (1) N24	0.90936	π* C23-S55	0.11225	20.72	0.42	0.119

Continued

NiB1	π^* C29-C33	0.02713	π^* C34-C35	0.38565	457.71	0.01	0.104
	π^* C28-C32	0.37837	π^* C34-C35	0.38565	407.37	0.01	0.104
	π^* C2-C3	0.42169	π^* C6-C9	0.39750	309.81	0.02	0.102
	π^* C2-C3	0.42169	π^* C7-C8	0.33601	196.74	0.02	0.101
ZnB1	π^* C2-C3	0.40891	π^* C6-C9	0.39186	369.37	0.01	0.102
	π^* C2- C3	0.40891	π^* C7-C8	0.32410	207.45	0.02	0.100
	LP(1)N24	1.79743	π^* C23-S55	0.26505	49.38	0.41	0.129
	πC7-C8	1.66904	π^* C2-C3	0.40891	36.08	0.37	0.106
MnB1	π^* C2-C3	0.20949	π^* C6-C9	0.19814	161.64	0.02	0.102
	π^* C28-C29	0.21041	π^* C32-C35	0.19844	154.73	0.02	0.102
	π^* C28-C29	0.21041	π^* C33-C34	0.16769	98.66	0.02	0.101
	π^* C2-C3	0.20949	π^* C7-C8	0.16666	97.93	0.02	0.100

4) Density of State (DOS) studies

The significance of the density of states (DOS) concept becomes is that, it serves as a powerful tool for unraveling intricate details about specific molecular orbitals. Moreover, the DOS approach unveils the distinct pattern exhibited by the Highest Occupied Molecular Orbital (HOMO) and Lowest Unoccupied Molecular Orbital (LUMO) [64]. To corroborate and solidify the outcomes derived from the frontier molecular orbital (FMO) analysis, which pertains to the biological reactivity of the investigated complexes and their potential to effectively interact with a receptor protein, a density of states (DOS) analysis was conducted [65]. At an energy level corresponding to the Fermi level of −0.1 eV, a detailed analysis of the electronic structure within MnB1 revealed an intriguing insight. The carbon fragment exhibited a pronounced peak within the valence orbital, highlighting its substantial contribution to the electronic arrangement. Concurrently, a significant peak emerges from the hydrogen fragment, contributing further complexity to the electronic landscape. However, a deeper examination reveals that the carbon fragment not only manifest a remarkable peak but also holds the highest charge density contribution closest to the valence level that aligns with the Fermi energy. This underscores the intricate balance of charge dynamics. In this context, the Mn fragment's electronic influence becomes evident, characterized by a conspicuous peak at 0.5 eV, corresponding to a transition into the conduction band. This peak's prominence underscores the material's electronic behavior as it crosses into the conduction band. For NiB1, a different narrative unfolds. Here, the Ni fragment exerts its dominance over the Highest Occupied Molecular Orbital (HOMO), whereas the role of the carbon atom shifts to that of the Lowest Unoccupied Molecular Orbital (LUMO). This contrast signifies a notable redistribution of charge density within this complex, unlike the pattern observed in MnB1. This intriguing observation hints at the occurrence of back bonding interactions within the NiB1 complex, pointing towards a distinct electronic communication pathway. Intriguingly, a similar pattern emerges in the ZnB1 complex, wherein the metal atom

(Zn), in this case engages in interaction with the carbon atom. This recurrent observation underscores a consistent theme of charge density distribution occurring between the carbon-metal interactions, showcasing a recurring hotspot of electronic interplay. Collectively, these results converge to reveal a pivotal finding the active site for potential ligand-protein interactions. This charge-dense domain, situated at the juncture of carbon-metal interactions, emerges as a focal point, hinting at its classification as a prospective interacting site—a vital insight for further understanding the intricate molecular interactions within these complexes.

3.8. Visual Studies

3.8.1. Quantum Theory of Atom-in-Molecule (QTAIM)

The quantum theory of atoms in molecules employs a topological analysis to investigate the interactions between atoms within a molecular system, based on the distribution of electron densities [66]. This analysis centers on bond critical points (BCPs). A bond critical point (BCP) is designated as (3, −1) and is considered indicative of a bonding relationship between two atoms. This is due to its distinctive features: two negative curvatures (maximum) and one positive curvature (minimum) [67]. The investigation was conducted computationally, focusing on various topological parameters such as electron density ρ(r), Lagrangian kinetic energy G(r), Hamiltonian kinetic energy K(r), potential energy density V(r), energy density H(r), electron (EFL), and the Laplacian of the electron density $V^2\rho$(r). From **Table 5** all the systems B1, CuB1, MnB1, and ZnB1 possess positive Laplacian of electron density ($\nabla^2\rho$(r)), suggesting closed-shell interactions (non-covalent) and average hydrogen bonding in all these systems. Furthermore, it is noteworthy that the nature of the bond H(r) is predominantly positive, indicating ionic bonds in all cases except for ZnB1 (S_{55}-Zn_{57} and S_{56}-Zn_{57}), where there is a negative energy density in H(r), signifying a covalent bond. Additionally, the observed elliplicity (ε) values for these bonds in the systems are less than 0.5, indicating stability.

Table 5. The topological parameter of the Ligand and its metal (II) complexes.

Compound	Bond	ρ (r)	$\nabla^2\rho$(r)	G(r)	V(r)	H(r)	G(r)/| V(r)|	ε
B1	N_{24}-C_{18}	0.1177	0.6375	0.1236	−0.8788	0.3574	−0.1406	0.9110
CuB1	S_{56}-Cu_{57}	0.5637	0.4934	0.1027	−0.8194	0.2071	−0.1253	0.0707
	Cl_{53}-Cu_{57}	0.4635	0.4397	0.8826	−0.6659	0.2166	−1.3254	0.0300
	N_{47}-Cu_{57}	0.5287	0.5898	0.1138	−0.8023	0.3361	−0.1418	0.0073
	S_{55}-Cu_{57}	0.5635	0.4919	0.1022	−0.8151	0.2073	−0.1253	0.0549
	CI_{54}-Cu_{57}	0.4627	0.4404	0.8797	−0.6583	0.2214	−1.3363	0.0693
	N_{21}-Cu_{57}	0.5311	0.5938	0.1145	−0.8069	0.3389	−0.1419	0.0081
MnB1	S_{56}-Mn_{57}	0.3430	0.1386	0.3159	−0.2853	0.3063	−1.1073	0.0368
	CI_{53}-Mn_{57}	0.4262	0.2430	0.5245	−0.4415	0.8298	−1.1879	0.0167
	S_{55}-Mn_{57}	0.3499	0.1427	0.3252	−0.2934	0.3176	−1.1083	0.0392
	CI_{54}-Mn_{57}	0.4704	0.2805	0.6068	−0.5126	0.9431	1.1837	0.0045

Continued

ZnB1	CI_{54}-Zn_{57}	0.4359	0.2438	0.5586	−0.5077	0.5087	−1.1003	0.03202
	CI_{53}-Zn_{57}	0.4032	0.1839	0.4503	−0.4408	0.9458	−1.0216	0.03236
	S_{55}-Zn_{57}	0.4217	0.2490	0.2093	−0.3564	−0.1470	−0.5872	0.09224
	S_{56}-Zn_{57}	0.4271	0.1087	0.3422	−0.4128	−0.7054	−0.8289	0.02496

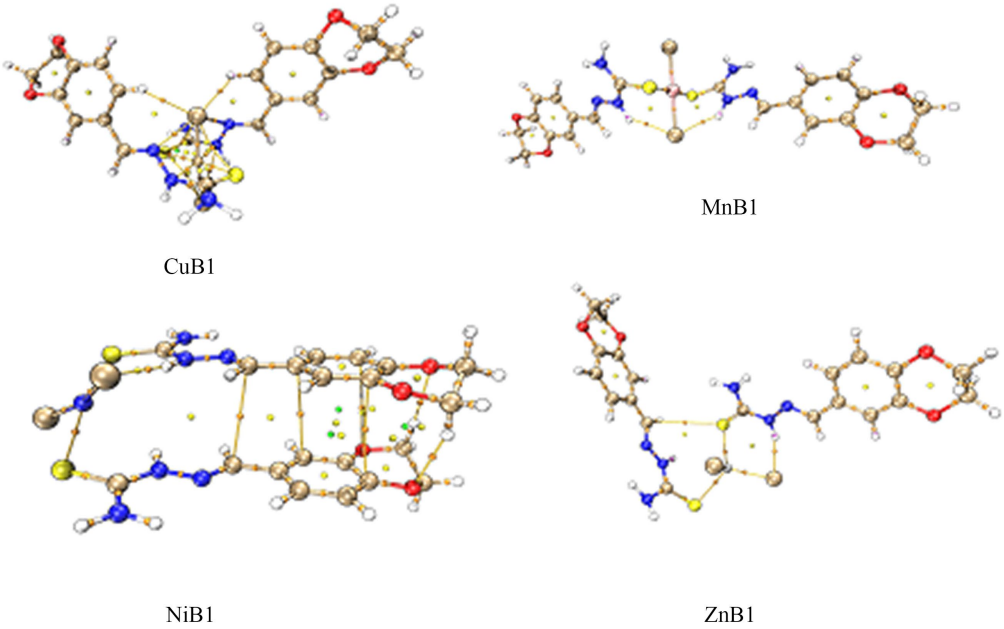

Figure 4. Graphical representation of the aim featuring the CP interactions present in the metal (II) complexes.

3.8.2. Non-Covalent Interaction (NCI)

The analysis of the non-covalent interaction index (NCI) based on the electron density and its gradient can be used to effectively distinguish and characterize these interactions in real space [68]. This method could be employed to investigate the type and intensity of interactions that occur between different species. Addressing this challenge, researchers have employed reduced density gradient (RDG) iso-surface studies to visually depict intramolecular interactions within the framework of NCI theory [69]. The simulated NCI result is presented in an RDG plot and the product of the second eigenvalue of the hessian matrix (λ_2) with the electron density sign (λ_2) ρ are reported in **Figure 4.** In CuB1, the central region of the two structures exhibited a combination of steric, van der Waals, and hydrogen interactions. This is due to the high electronegativity of the metal and chlorine atoms present in this region. Additionally, steric interactions are observed at the center of the benzene rings in this structure, which is attributed to the carbon atoms. MnB1 and ZnB1 exhibit similar interactions as observed in CuB1, except for NiB1 where a considerable amount of van der Waals interactions are noticeable. This shows that NiB1 plays a crucial role in determining the specificity and affinity of the interaction with biological system.

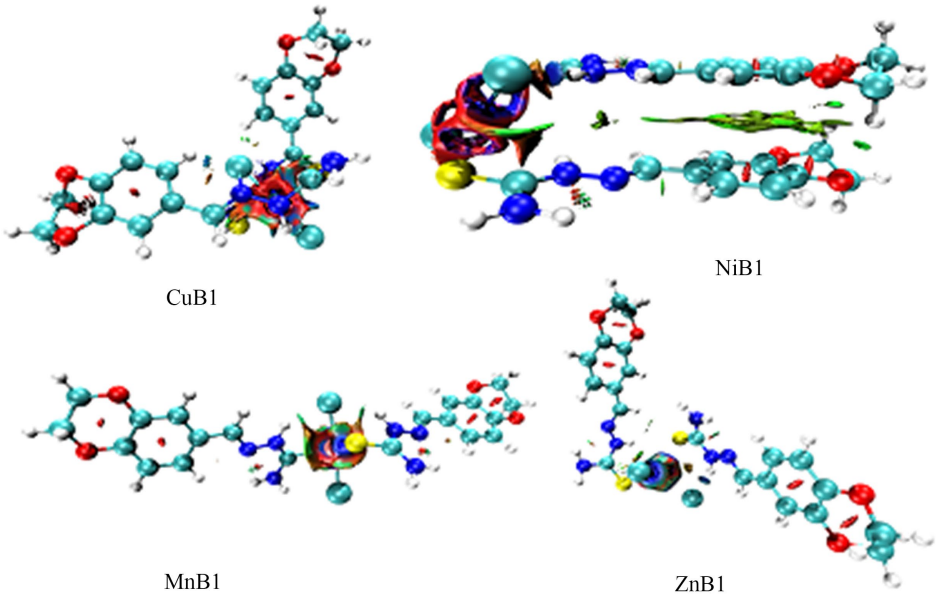

Figure 5. Pictorial representation of the 2D plots of the non-covalent interaction studied interaction.

3.9. Löwdin Charge Analysis

The Löwdin charge analysis, also known as Löwdin population analysis, is a fundamental tool within computational chemistry. It plays a crucial role in breaking down the overall electron density of a molecule into distinct contributions that originate from specific atoms or atom groups [70]. The outcomes of the Löwdin charge analysis from this investigation have been presented in **Table 6**. The table encompasses details like d-orbital degeneracy, d-orbital population, and the overall net charge of the studied system. The interaction between the studied complexes and their ligands resulted in the removal of degeneracy, giving rise to a phenomenon known as crystal field splitting. This phenomenon causes the d-orbitals to separate into distinct energy levels, thus generating a lower-energy orbital set (t_{2g}) and a higher-energy orbital set (e_g). The analysis involves the d-orbital occupancies and net charges (QNet) for each system, along with separate results for spin-up (↑) and spin-down (↓) electrons. In CuB1, the net charge for the transition metal (TM) in this system is essentially zero (0.00001). The d-orbital occupancy values calculated is 6.952 and the d-orbital occupancy values for the spin-up, spin-down state are given for each of the d orbitals. Similar interpretations can be made for the remaining systems (MnB1, NiB1, ZnB1). The key points to consider are the orbital occupancies and the net charge on the transition metal. The differences in d-orbital occupancies between spin-up and spin-down states suggest differences in electronic configurations due to spin polarization. The net charge (QNet) values represent the difference between the total number of electrons associated with the transition metal and its expected valence electron count. In most cases, the net charge should be close to zero, indicating that the system is electrically neutral. Also, the net Löwdin charges provide a consistent observation

that the transition metals maintain approximately neutral charges within these complexes, suggesting that they are participating in typical coordination interactions without substantial electron transfer. The observed differences in d-orbital occupancy patterns can provide insights into the electronic structure and reactivity of these transition metal complexes. These differences might lead to varied magnetic behavior, redox properties, and catalytic activities. The consistent neutrality of the transition metal charges suggests that these systems are likely to engage in coordination chemistry without extreme electron transfer, which is essential for their roles in catalysis and other chemical processes.

Table 6. Degeneracy of the d-orbital, occupancy and the total net charge of the studied interactions.

Compound	d_{xy}	d_{xz}	d_{yz}	$d_{x^2-y^2}$	d_{z^2}	d-occupancy	$Q_{Net}(TM)$
CuB1	---	---	---	---	---	6.95202	0.00001
Spin up (↑)	0.52615	0.89440	0.64831	1.17885	0.04196	---	---
Spin down (↓)	0.49058	0.49027	0.48417	0.49027	0.51217	---	---
MnB1	---	---	---	---	---	6.06872	0.00000014
Spin up (↑)	1.02316	1.33762	0.64314	0.23880	0.73807	---	---
Spin down (↓)	0.50328	0.49810	0.50235	0.25752	0.32668	---	---
NiB1	---	---	---	---	---	8.7633	0.00000013
Spin up (↑)	0.98036	1.10303	1.29762	1.43353	1.46890	---	---
Spin down (↓)	0.49558	0.49652	0.48435	0.49837	0.50501	---	---
ZnB1	---	---	---	---	---	10.0342	0.00000016
Spin up (↑)	1.60834	1.60984	1.61104	1.61271	1.61029	---	---
Spin down (↓)	0.39513	0.39495	0.39679	0.39903	0.39608	---	---

3.10. Molecular Docking Studies

An essential computational method in the field of molecular biology, molecular docking supports drug design in particular [71]. Predicting how a complex will interact with a known protein structure is the primary goal of protein-ligand docking. In order to obtain insight into a synthesized compounds' potential as an antifungal medication against candidiasis, virtual screening was done using molecular docking. The over-the-counter medication fluconazole (access code DB00196) was used as a benchmark for comparison because, it has a variety of side effects, including skin rashes, allergic reactions, diarrhea, and constipation. Inspired by the search for a new antifungal substance, binding affinities, which reflect the strength of interactions between the protein and ligand and so determine stability and reactivity, were at the center of the investigation. As shown in Table 7, the binding affinities for NIB1, CuB1, ZnB1, MnB1, and B1 are, −8.2 kcal/mol, −8.1 kcal/mol, −8 kcal/mol, −7.9 kcal/mol, and −7.1 kcal/mol respectively. Notably, B1 showed the poorest connection, followed by CuB1, ZnB, and MnB1, with NiB1 showing

the greatest affinity. Fluconazole, on the other hand, showed a theoretical binding affinity of −8.2 kcal/mol. The impressive result demonstrated the protein receptor (5BTH) and our compounds' stronger binding capacity. It's interesting to note that, FLUC and NiB1 had the same binding affinities of −8.2 kcal/mol, highlighting NiB1's potential. Additionally, the mean binding affinities of our examined complexes; NiB1, CuB1, ZnB1, and MnB1 were noticeably higher of −7.93 kcal/mol, −7.77 kcal/mol, −7.54 kcal/mol, and −7.68 kcal/mol, respectively, an indication of the reactive and stable nature of the metal complexes. From this it was clear that hydrogen bonds played a critical role in molecular interactions and complex integrity. With the proteins 5BTH (LYS A: 134, LYS A: 134), CuB1 (LEU A: 122), ZnB1 (THR A:360), and B1 (LEU A:350), MnB1 consistently established hydrogen bonds. Surprisingly, the number of hydrogen bonds formed between fluconazole and protein 5BTH were somewhat higher (SER A: 41, ILE A: 224, GLU A: 174). As show in Figure 4 and Figure 5, small bond distances were profoundly significant because, they indicated strong non-covalent interactions including hydrogen bonds, ionic interactions, and van der Waals forces. The protein-ligand complex's stability and specificity were strengthened by these interactions. This understanding was significant when calculating the average hydrogen bond distances, with B1 and CuB1 exhibiting increased reactivity at an average bond distance of 1.73 and MnB1 coming in second, at 1.86. The usual medication, in contrast, showed a distance of 2.38 kcal/mol. The conclusion that emerged when mean binding affinities, binding affinity, and bond distance values were taken into account was that, the prepared compounds demonstrated more pronounced biological activity and reactivity in their interactions with the 5BTH protein than fluconazole.

Table 7. Amino acid residue and binding affinities of protein-ligand interaction.

Compound	Amino acid residue	Binding affinity (kcal/mol)	Bon distances (Å)	Mean binding affinity (kcal/mol)
B1 + 5BTH	LEU A: 350	−7.1	1.73	−6.48
CuB1 + 5BTH	LEU A: 122	−8.1	1.73	−7.77
MnB1 + 5BTH	LYSA: 134, ARG A: 349	−7.9	1.86, 2.83	−7.68
NiB1 + 5BTH	ARG A: 349	−8.2	2.15	−7.93
ZnB1 + 5BTH	THR A: 360	−8	1.82	−7.54
FLUC + 5BTH	SER A: 41, ILEA: 224, GLU A: 174	−8.2	2.38, 2.68, 2.54	−7.03

4. Conclusions

In this paper, a new ligand 1, 4-benzodioxane-6-carboxaldehyde thiosemicarbazone (B1) and its Zn(II), Cu(II), Ni(II) and Mn(II) complexes were synthesized and characterized by various spectroscopic techniques (Figure 6). The ligand and its metal complexes were theoretically investigated for their biological activity

against *Candida albicans* using Density Functional Theory (DFT) at the WB97XD functional, employing the 6-311++G (d,p) basis set. The ligand 1, 4-benzodioxane-6-carboxaldehyde thiosemicarbazone (B1) and its metal complexes exhibit promising activity against *Candida albicans* as compared to the drug Fluconazole. It is interesting to note that Fluconazole, the standard drug and Ni(II) complex had the same binding affinity value of −8.2 kcal/mol, highlighting NiB1's potential. Additionally, compared to standard drug Fluconazole, the results demonstrated that the protein receptor (5BTH) and the nickel complex had a strong binding capacity.

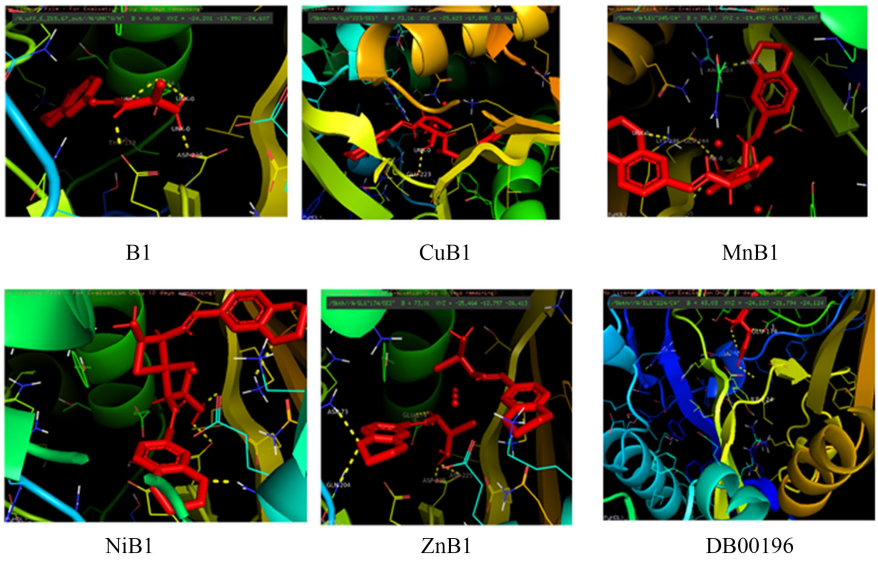

Figure 6. Visualization of the interaction of Fluconazole (FLUC) with 7P3R and 1,4-benzodioxane-6-carboxaldehyde thiosemicarbazone (B1) interactions with 7P3R and 1XTC.

Acknowledgments

The authors gratefully acknowledge Professor Zou Jinglin of the State Key Laboratory of Coordination Chemistry, Nanjing University, P. R. China for the spectral analyses.

Conflicts of Interest

The authors declare no conflicts of interest regarding the publication of this paper.

References

[1] Valand, N., Gazioglu, O., Yesilkaya, H., Shivkumar, M., Horley, N., Arroo, R., *et al.* (2023) Interactions of Candida Tropicalis pH-Related Antigen 1 with Complement Proteins C3, C3b, Factor-H, C4BP and Complement Evasion. *Immunobiology*, **228**, Article ID: 152303. https://doi.org/10.1016/j.imbio.2022.152303

[2] Hani, U., Shivakumar, H., Vaghela, R., M. Osmani, R. and Shrivastava, A. (2015) Candidiasis: A Fungal Infection—Current Challenges and Progress in Prevention and Treatment. *Infectious Disorders-Drug Targets*, **15**, 42-52. https://doi.org/10.2174/1871526515666150320162036

[3] Launder, D., Dillon, J.T., Wuescher, L.M., Glanz, T., Abdul-Aziz, N., Yi, E.M., *et al.* (2024) Immunity to Pathogenic Mucosal *C. albicans* Infections Mediated by Oral Megakaryocytes Activated by IL-17 and Candidalysin. *Mucosal Immunology*, **17**, 182-200. https://doi.org/10.1016/j.mucimm.2024.01.003

[4] Alfaifi, A.A., Wang, T.W., Perez, P., Sultan, A.S., Meiller, T.F., Rock, P., *et al.* (2024) SARS-CoV-2 Infection of Salivary Glands Compromises the Production of a Secreted Antifungal Peptide with Potential Implications for Development of Oral Candidiasis. *PLOS Pathogens*, **20**, e1012375. https://doi.org/10.1371/journal.ppat.1012375

[5] Samaranayake, L.P. (1992) Oral Mycoses in HIV Infection: A Review. *Oral Surgery, Oral Medicine, Oral Pathology*, **73**, 171-180. https://doi.org/10.1016/0030-4220(92)90191-r

[6] Kullberg, B.J. and Arendrup, M.C. (2015) Invasive Candidiasis. *New England Journal of Medicine*, **373**, 1445-1456. https://doi.org/10.1056/nejmra1315399

[7] Cleveland, A.A., Farley, M.M., Harrison, L.H., Stein, B., Hollick, R., Lockhart, S.R., *et al.* (2012) Changes in Incidence and Antifungal Drug Resistance in Candidemia: Results from Population-Based Laboratory Surveillance in Atlanta and Baltimore, 2008-2011. *Clinical Infectious Diseases*, **55**, 1352-1361. https://doi.org/10.1093/cid/cis697

[8] Berkow, E. and Lockhart, S. (2017) Fluconazole Resistance in Candida Species: A Current Perspective. *Infection and Drug Resistance*, **10**, 237-245. https://doi.org/10.2147/idr.s118892

[9] Pfaller, M.A., Rhomberg, P.R., Messer, S.A., Jones, R.N. and Castanheira, M. (2015) Isavuconazole, Micafungin, and 8 Comparator Antifungal Agents' Susceptibility Profiles for Common and Uncommon Opportunistic Fungi Collected in 2013: Temporal Analysis of Antifungal Drug Resistance Using CLSI Species-Specific Clinical Breakpoints and Proposed Epidemiological Cutoff Values. *Diagnostic Microbiology and Infectious Disease*, **82**, 303-313. https://doi.org/10.1016/j.diagmicrobio.2015.04.008

[10] Srivastava, V., Singla, R.K. and Dubey, A.K. (2018) Emerging Virulence, Drug Resistance and Future Anti-Fungal Drugs for Candida Pathogens. *Current Topics in Medicinal Chemistry*, **18**, 759-778. https://doi.org/10.2174/1568026618666180528121707

[11] Lee, Y., Puumala, E., Robbins, N. and Cowen, L.E. (2020) Antifungal Drug Resistance: Molecular Mechanisms in *candida Albicans* and Beyond. *Chemical Reviews*, **121**, 3390-3411. https://doi.org/10.1021/acs.chemrev.0c00199

[12] Ahmed, B. and Khan, H.S. (2008) Chemistry and Pharmacology of Benzodioxanes, Organic Chemistry. *An Indian Journal*, *OCAIJ*, **4**, 65-77.

[13] Pilkington, L.I., Wagoner, J., Polyak, S.J. and Barker, D. (2015) Enantioselective Synthesis, Stereochemical Correction, and Biological Investigation of the Rodgersinine Family of 1,4-Benzodioxane Neolignans. *Organic Letters*, **17**, 1046-1049. https://doi.org/10.1021/acs.orglett.5b00189

[14] Idris, N., Anderson, A.J. and Bakare, O. (2022) Synthesis and Characterization of 1,4-Benzodioxane-6-Carboxylic Acid Amide Analogs. *International Journal of Organic Chemistry*, **12**, 143-160. https://doi.org/10.4236/ijoc.2022.123012

[15] Erceg, M., Vertzoni, M., Cerić, H., Dumić, M., Cetina-Čižmek, B. and Reppas, C. (2012) *In Vitro* vs. Canine Data for Assessing Early Exposure of Doxazosin Base and Its Mesylate Salt. *European Journal of Pharmaceutics and Biopharmaceutics*, **80**, 402-409. https://doi.org/10.1016/j.ejpb.2011.10.004

[16] Fang, Q.K., Grover, P., Han, Z., McConville, F.X., Rossi, R.F., Olsson, D.J., *et al.* (2001) Practical Chemical and Enzymatic Technologies for (s)-1,4-Benzodioxan-2-Carboxypiperizine Intermediate in the Synthesis of (s)-Doxazosin Mesylate. *Tetrahedron: Asymmetry*, **12**, 2169-2174. https://doi.org/10.1016/s0957-4166(01)00368-8

[17] Song, X., Yang, Y., Zhao, J. and Chen, Y. (2014) Synthesis and Antibacterial Activity of Cinnamaldehyde Acylhydrazone with a 1,4-Benzodioxan Fragment as a Novel Class of Potent β-Ketoacyl-Acyl Carrier Protein Synthase III (FabH) Inhibitor. *Chemical and Pharmaceutical Bulletin*, **62**, 1110-1118. https://doi.org/10.1248/cpb.c14-00485

[18] Vazquez, M.T., Rosell, G. and Pujol, M.D. (1996) Synthesis and Anti-Inflammatory Activity of 2,3-Dihydro-1,4-benzodioxin Methyl Carboxylic Acids. *Farmaco*, **51**, 215-217.

[19] Vázquez, M.T., Rosell, G. and Pujol, M.D. (1997) Synthesis and Anti-Inflammatory Activity of Rac-2-(2,3-Dihydro-1,4-Benzodioxin)propionic Acid and Its R and S Enantiomers. *European Journal of Medicinal Chemistry*, **32**, 529-534. https://doi.org/10.1016/s0223-5234(97)84016-0

[20] Xu, M.Z., Lee, W.S., Han, J.M., Oh, H.W., Park, D.S., Tian, G.R., *et al.* (2006) Antioxidant and Anti-Inflammatory Activities of N-Acetyldopamine Dimers from Periostracum Cicadae. *Bioorganic & Medicinal Chemistry*, **14**, 7826-7834. https://doi.org/10.1016/j.bmc.2006.07.063

[21] Nfor, E.N., Liu, W., Zuo, J.L., You, X.Z., Offiong, E.O. and Eno, E.A. (2006) Synthesis, Crystal Structure Luminescent Property of Novel μ-Thioyanato-bis-(2-acetylpyridine-thiosemicarbazonato)(thiocyanato) Cadmium(II) Complex. *Transition Metal Chemistry*, **31**, 837-841.

[22] Nfor, E.N., Liu, W., Zuo, J., You, X. and Offiong, O.E. (2006) Di-μ-acetato-bis[(2-acetylpyridine thiosemicarbazonato)Zinc(II)]. *Acta Crystallographica Section C Crystal Structure Communications*, **62**, m211-m213. https://doi.org/10.1107/s0108270106009152

[23] Nfor, E.N. and Majoumo-Mbe, F. (2016) Synthesis, Crystal and Molecular Structure of Manganese(II) Complex of 2-Acetylpyridine N(4) Ethylthiosemicarbazone. *Communications in Inorganic Synthesis*, **4**, 5-11.

[24] Aly, M.M., Mohamed, Y.A., El-Bayouki, K.A.M., Basyouni, W.M. and Abbas, S.Y. (2010) Synthesis of Some New 4(3h)-Quinazolinone-2-Carboxaldehyde Thiosemicarbazones and Their Metal Complexes and a Study on Their Anticonvulsant, Analgesic, Cytotoxic and Antimicrobial Activities—Part-1. *European Journal of Medicinal Chemistry*, **45**, 3365-3373. https://doi.org/10.1016/j.ejmech.2010.04.020

[25] Viñuelas-Zahínos, E., Luna-Giles, F., Torres-García, P. and Fernández-Calderón, M.C. (2011) Co(III), Ni(II), Zn(II) and Cd(II) Complexes with 2-Acetyl-2-Thiazoline Thiosemicarbazone: Synthesis, Characterization, X-Ray Structures and Antibacterial Activity. *European Journal of Medicinal Chemistry*, **46**, 150-159. https://doi.org/10.1016/j.ejmech.2010.10.030

[26] Halder, S., Paul, P., Peng, S., Lee, G., Mukherjee, A., Dutta, S., *et al.* (2012) Benzaldehyde Thiosemicarbazone Complexes of Platinum: Syntheses, Structures and Cytotoxic Properties. *Polyhedron*, **45**, 177-184. https://doi.org/10.1016/j.poly.2012.07.037

[27] Sampath, K., Sathiyaraj, S., Raja, G. and Jayabalakrishnan, C. (2013) Mixed Ligand Ruthenium(III) Complexes of Benzaldehyde 4-Methyl-3-Thiosemicarbazones with Triphenylphosphine/Triphenylarsine Co-Ligands: Synthesis, DNA Binding, DNA Cleavage, Antioxidative and Cytotoxic Activity. *Journal of Molecular Structure*, **1046**, 82-91. https://doi.org/10.1016/j.molstruc.2013.04.051

[28] Chandra, S., Bargujar, S., Nirwal, R. and Yadav, N. (2013) Synthesis, Spectral Characterization and Biological Evaluation of Copper(II) and Nickel(II) Complexes with Thiosemicarbazones Derived from a Bidentate Schiff Base. *Spectrochimica Acta Part A*: *Molecular and Biomolecular Spectroscopy*, **106**, 91-98.

https://doi.org/10.1016/j.saa.2012.12.014

[29] Emori, W., Louis, H., Adalikwu, S.A., Timothy, R.A., Cheng, C., Gber, T.E., *et al.* (2022) Molecular Modeling of the Spectroscopic, Structural, and Bioactive Potential of Tetrahydropalmatine: Insight from Experimental and Theoretical Approach. *Polycyclic Aromatic Compounds*, **43**, 5958-5975. https://doi.org/10.1080/10406638.2022.2110908

[30] Rao, A.V., Benson, D.A., Darby, C., Patterson, M.A., Francolin, C., Sanders, I., *et al.* (2010) Algorithm 902: Gpops, a Matlab Software for Solving Multiple-Phase Optimal Control Problems Using the Gauss Pseudospectral Method. *ACM Transactions on Mathematical Software*, **37**, 1-39. https://doi.org/10.1145/1731022.1731032

[31] Jacques, A.A., Soleymane, K., Sékou, D. and Sawaliho, E.B.E. (2022) NBO Analysis by ONIOM and DFT (B3LYP) Calculations of Intramolecular and Intermolecular Interactions of Artemisinin, Quinine and Thirteen Manzamenones with H_2O or Alanine. *Journal of Materials Science and Chemical Engineering*, **10**, 78-98. https://doi.org/10.4236/msce.2022.1010006

[32] Agwamba, E.C., Louis, H., Unimuke, T.O., Ameuru, U.S., Mathias, G.E., Chukwu, U.G., *et al.* (2022) Molecular Modeling of the Photovoltaic Properties of Amino Naphthalene and N-Alkylated-Isoquinoline Dye. *Journal of the Indian Chemical Society*, **99**, Article ID: 100739. https://doi.org/10.1016/j.jics.2022.100739

[33] Tahir, R., Kennedy, A., Elsea, S.H. and Dickinson, A.J. (2014) Retinoic Acid Induced-1 (rai1) Regulates Craniofacial and Brain Development in Xenopus. *Mechanisms of Development*, **133**, 91-104. https://doi.org/10.1016/j.mod.2014.05.004

[34] Adams, D.R., Yuan, H., Holyoak, T., Arajs, K.H., Hakimi, P., Markello, T.C., *et al.* (2014) Three Rare Diseases in One Sib Pair: RAI1, PCK1, GRIN2B Mutations Associated with Smith-Magenis Syndrome, Cytosolic PEPCK Deficiency and NMDA Receptor Glutamate Insensitivity. *Molecular Genetics and Metabolism*, **113**, 161-170. https://doi.org/10.1016/j.ymgme.2014.04.001

[35] Shaweta, S., Akhil, S. and Utsav, G. (2021) Molecular Docking Studies on the Anti-Fungal Activity of *Allium sativum* (Garlic) against Mucormycosis (Black Fungus) by BIOVIA Discovery Studio Visualizer 21.1.0.0. *Annals of Antivirals and Antiretrovirals*, **5**, 28-32. https://doi.org/10.17352/aaa.000013

[36] Kondapuram, S.K., Sarvagalla, S. and Coumar, M.S. (2021) Docking-Based Virtual Screening Using Pyrx Tool: Autophagy Target Vps34 as a Case Study. In: Coumar, M.S., Ed., *Molecular Docking for Computer-Aided Drug Design*, Elsevier, 463-477. https://doi.org/10.1016/b978-0-12-822312-3.00019-9

[37] Nibbering, E.T.J. and Elsaesser, T. (2004) Ultrafast Vibrational Dynamics of Hydrogen Bonds in the Condensed Phase. *Chemical Reviews*, **104**, 1887-1914. https://doi.org/10.1021/cr020694p

[38] Bulusu, G. and Desiraju, G.R. (2019) Strong and Weak Hydrogen Bonds in Protein-ligand Recognition. *Journal of the Indian Institute of Science*, **100**, 31-41. https://doi.org/10.1007/s41745-019-00141-9

[39] Geary, W.J. (1971) The Use of Conductivity Measurements in Organic Solvents for the Characterisation of Coordination Compounds. *Coordination Chemistry Reviews*, **7**, 81-122. https://doi.org/10.1016/s0010-8545(00)80009-0

[40] Ali, I., Wani, W.A. and Saleem, K. (2013) Empirical Formulae to Molecular Structures of Metal Complexes by Molar Conductance. *Synthesis and Reactivity in Inorganic, Metal-Organic, and Nano-Metal Chemistry*, **43**, 1162-1170. https://doi.org/10.1080/15533174.2012.756898

[41] Li, M.X., Chen, C.L., Zhang, D., Niu, J.Y. and Ji, B.S. (2011) Synthesis, Crystal Structures, and Biological Evaluation of Manganese(II) and Nickel(II) Complexes of 4-Cyclohexyl-1-(1-(pyrazin-2-yl)ethylidene) Thiosemicarbazide. *European Journal of Medicinal Chemistry*, **45**, 3169.

[42] Beckford, F.A., Leblanc, G., Thessing, J., Shaloski, M., Frost, B.J., Li, L., *et al.* (2009) Organometallic Ruthenium Complexes with Thiosemicarbazone Ligands: Synthesis, Structure and Cytotoxicity of [(η6-p-cymene)Ru(NS)Cl]+ (NS = 9-Anthraldehyde Thiosemicarbazones). *Inorganic Chemistry Communications*, **12**, 1094-1098. https://doi.org/10.1016/j.inoche.2009.08.034

[43] Joseph, M., Kuriakose, M., Kurup, M.R.P., Suresh, E., Kishore, A. and Bhat, S.G. (2006) Structural, Antimicrobial and Spectral Studies of Copper(II) Complexes of 2-Benzoylpyridine N(4)-Phenyl Thiosemicarbazone. *Polyhedron*, **25**, 61-70. https://doi.org/10.1016/j.poly.2005.07.006

[44] Lobana, T.S., Kumari, P. and Butcher, R.J. (2008) Cyclopentanone Thiosemicarbazone (Hcptsc) Induces a New Bonding Pattern in (Ph3P) Cu(μ-Br)(μ3-S, N-Hcptsc) CuBr (PPh3) Dimer. *Inorganic Chemistry Communications*, **11**, 11-14. https://doi.org/10.1016/j.inoche.2007.10.001

[45] Nakamato, K. (1971) Infrared and Raman Spectra of Inorganic and Coordination Compounds. Wiley-Inter Science.

[46] Raja, M.U., Sindhuja, E. and Ramesh, R. (2010) Arene Ruthenium(II) P-Chloroacetophenone Phenylthiosemicarbazone Complex Mediated Transfer Hydrogenation of Ketones. *Inorganic Chemistry Communications*, **13**, 1321-1324. https://doi.org/10.1016/j.inoche.2010.07.026

[47] Mikwa, C.C., Toh-Boyo, G.M., Njong, R.N., Ndoye, B.N., Ndamyabera, C.A., Katsuumi, N., *et al.* (2022) Bivalent Metal Complexes of a Novel Modified Nicotinic Acid Hydrazide Drug: Synthesis, Characterization, and Anti-Tubercular Studies. *European Journal of Chemistry*, **13**, 63-68. https://doi.org/10.5155/eurjchem.13.1.63-68.2183

[48] Nfor, E.N., Husian, A., Majoumo-Mbe, F., Njah, I.N., Offiong, O.E. and Bourne, S.A. (2013) Synthesis, Crystal Structure and Antifungal Activity of a Ni(II) Complex of a New Hydrazone Derived from Antihypertensive Drug Hydralazine Hydrochloride. *Polyhedron*, **63**, 207-213. https://doi.org/10.1016/j.poly.2013.07.028

[49] İlhan-Ceylan, B., Bolukbasi, O., Yilmaz, A., Kaya, K., Kurt, Y. and Ülküseven, B. (2021) Synthesis, Spectroscopic Characterization and Quantum Chemical Studies of a Dioxomolybdenum(VI) Complex with an N,S-Substituted Pyridoxal Thiosemicarbazone. *Polyhedron*, **193**, Article ID: 114884. https://doi.org/10.1016/j.poly.2020.114884

[50] Şen, B., Kalhan, H.K., Demir, V., Güler, E.E., Kayalı, H.A. and Subaşı, E. (2019) Crystal Structures, Spectroscopic Properties of New Cobalt(II), Nickel(II), Zinc(II) and Palladium(II) Complexes Derived from 2-Acetyl-5-Chloro Thiophene Thiosemicarbazone: Anticancer Evaluation. *Materials Science and Engineering: C*, **98**, 550-559. https://doi.org/10.1016/j.msec.2018.12.080

[51] Fousiamol, M.M., Sithambaresan, M., Damodaran, K.K. and Kurup, M.R.P. (2020) Syntheses, Spectral Aspects and Biological Studies of Bromide and Azide Bridged Box Dimer Copper(II) Complexes of an NNO Donor Aroylhydrazone. *Inorganica Chimica Acta*, **501**, Article ID: 119301. https://doi.org/10.1016/j.ica.2019.119301

[52] Ayad, M., Schollhammer, P., Le Mest, Y., Wojcik, L., Pétillon, F.Y., Le Poul, N., *et al.* (2019) Mononuclear Copper(II) Complexes Containing a Macrocyclic Ditopic Ligand: Synthesis, Structures and Properties. *Inorganica Chimica Acta*, **497**, Article ID:

119081. https://doi.org/10.1016/j.ica.2019.119081

[53] Emara, A.A.A., Saleh, A.A. and Adly, O.M.I. (2007) Spectroscopic Investigations of New Binuclear Transition Metal Complexes of Schiff Bases Derived from 4,6-Diacetylresorcinol and 3-Amino-1-Propanol or 1,3-Diamino-Propane. *Spectrochimica Acta Part A*: *Molecular and Biomolecular Spectroscopy*, **68**, 592-604. https://doi.org/10.1016/j.saa.2006.12.034

[54] Reshma, G., Padmanabhan, V., Varma, A.R., Gouri, M.S., Nair, U.R., Parvathy, P.B., *et al.* (2021) Synthesis and Structure of Mono and Bis{1,3-Bis(2-Pyridylimino)isoindoline} Supported 3d Transition Metal Complexes. *Journal of Molecular Structure*, **1226**, Article ID: 129344. https://doi.org/10.1016/j.molstruc.2020.129344

[55] AbouEl-Enein, S.A., Emam, S.M., Wagdy, R.M. and Abouzayed, F.I. (2020) Spectral and Thermal Investigation of Novel Biologically Active (n-(1,5-Dimethyl-3-Oxo-2-Phenyl-2,3-Dihydro-1h-Pyrazol-4-Yl)-2-(1,5-Dimethyl-3-Oxo-2-Phenyl-2,3-Dihydro-1h-Pyrazol-4-Yl-Amino)-2-Oxo-Cetimidic Acid) Ligand and Its Metal Complexes. *Journal of Molecular Structure*, **1215**, Article ID: 128230. https://doi.org/10.1016/j.molstruc.2020.128230

[56] Mashaly, M.M., Ismail, T.M., El-Maraghy, S.B. and Habib, H.A. (2004) Heteronuclear Complexes of Oxorhenium(V) with Fe(III), Co(II), Ni(II), Cu(II), Cd(II) and UO2(VI) and Their Biological Activities. *Journal of Coordination Chemistry*, **57**, 1099-1123. https://doi.org/10.1080/00958970412331281881

[57] Shebl, M., Khalil, S.M.E., Kishk, M.A.A., El-Mekkawi, D.M. and Saif, M. (2019) New Less Toxic Zeolite-Encapsulated Cu(II) Complex Nanomaterial for Dual Applications in Biomedical Field and Wastewater Remediation. *Applied Organometallic Chemistry*, **33**, e5147. https://doi.org/10.1002/aoc.5147

[58] Cotton F.A. and Wilkinson, G. (1980) Advanced Inorganic Chemistry. 4th Edition, John Wiley and Sons.

[59] Nataf, L., Rodríguez, F., Valiente, R. and González, J. (2009) Spectroscopic and Luminescence Properties of (CH3)4NMnCl3: A Sensitive Mn^{2+}-Based Pressure Gauge. *High Pressure Research*, **29**, 653-659. https://doi.org/10.1080/08957950903414979

[60] Shehzad, M.T., Khan, A., Islam, M., Hameed, A., Khiat, M., Halim, S.A., *et al.* (2020) Synthesis and Urease Inhibitory Activity of 1,4-Benzodioxane-Based Thiosemicarbazones: Biochemical and Computational Approach. *Journal of Molecular Structure*, **1209**, Article ID: 127922. https://doi.org/10.1016/j.molstruc.2020.127922

[61] Doust Mohammadi, M., Louis, H., Chukwu, U.G., Bhowmick, S., Rasaki, M.E. and Biskos, G. (2023) Gas-Phase Interaction of CO, CO_2, H_2S, NH_3, NO, NO_2, and SO_2 with $Zn_{12}O_{12}$ and Zn_{24} Atomic Clusters. *ACS Omega*, **8**, 20621-20633. https://doi.org/10.1021/acsomega.3c01177

[62] Eno, E.A., Okon, E.E.D., Louis, H., Obot, N.U., Adalikwu, S.A., Unimuke, T.O., *et al.* (2023) Synthesis, Spectral Characterization, DFT Studies, and Computational Screening of 4-Amino-3-mercapto-5-methyl-1,2,4-triazole and Its Cadmium(II) Mixed Ligands Complexes as Potential Antimalaria Drug. *Vietnam Journal of Chemistry*, **61**, 187-203. https://doi.org/10.1002/vjch.202200110

[63] Asogwa, F.C., Agwamba, E.C., Louis, H., Muozie, M.C., Benjamin, I., Gber, T.E., *et al.* (2022) Structural Benchmarking, Density Functional Theory Simulation, Spectroscopic Investigation and Molecular Docking of N-(1h-Pyrrol-2-Yl) Methylene)-4-Methylaniline as Castration-Resistant Prostate Cancer Chemotherapeutic Agent. *Chemical Physics Impact*, **5**, Article ID: 100091. https://doi.org/10.1016/j.chphi.2022.100091

[64] Benjamin, I., Udoikono, A.D., Louis, H., Agwamba, E.C., Unimuke, T.O., Owen,

A.E., *et al.* (2022) Antimalarial Potential of Naphthalene-Sulfonic Acid Derivatives: Molecular Electronic Properties, Vibrational Assignments, and *In-Silico* Molecular Docking Studies. *Journal of Molecular Structure*, **1264**, Article ID: 133298. https://doi.org/10.1016/j.molstruc.2022.133298

[65] Devi, C.U., Jayasutha, B. and Arivazhagan, M. (2021) Molecular Dynamic Simulations, Geometrical, and Vibrational Spectral Studies of *α*, *α*, *á*, *á* Tetra Bromo-m-xylene. *Annals of the Romanian Society for Cell Biology*, **25**, 10294-10310.

[66] Tan, S.T.M., Gumyusenge, A., Quill, T.J., LeCroy, G.S., Bonacchini, G.E., Denti, I., *et al.* (2022) Mixed Ionic-Electronic Conduction, a Multifunctional Property in Organic Conductors. *Advanced Materials*, **34**, Article ID: 2110406. https://doi.org/10.1002/adma.202110406

[67] Costa Júnior, A.C., Versiane, O., Faget Ondar, G., Ramos, J.M., Ferreira, G.B., Martin, A.A., *et al.* (2012) An Experimental and Theoretical Approach of Spectroscopic and Structural Properties of the Bis(diethyldithiocarbamate)-Cobalt(II). *Journal of Molecular Structure*, **1029**, 119-134. https://doi.org/10.1016/j.molstruc.2012.06.041

[68] Lu, T. and Chen, Q. (2021) Interaction Region Indicator: A Simple Real Space Function Clearly Revealing Both Chemical Bonds and Weak Interactions. *Chemistry-Methods*, **1**, 231-239. https://doi.org/10.1002/cmtd.202100007

[69] Ahsan, S.M.A., Al-Shaalan, N.H., Amin, M.R., Molla, M.R., Aktar, S., Alam, M.M., *et al.* (2020) Interaction of Moxifloxacin Hydrochloride with Sodium Dodecyl Sulfate and Tween 80: Conductivity & Phase Separation Methods. *Journal of Molecular Liquids*, **301**, Article ID: 112467. https://doi.org/10.1016/j.molliq.2020.112467

[70] Kamel, M., Morsali, A., Raissi, H. and Mohammadifard, K. (2020) Theoretical Insights into the Intermolecular and Mechanisms of Covalent Interaction of Flutamide Drug with COOH and COCl Functionalized Carbon Nanotubes: A DFT Approach. *Chemical Review and Letters*, **3**, 23-37.

[71] Reang, J., Yadav, V., Vinita, M.J., Sharma, P.C., Tonk, R.K., *et al.* (2023) Informatics: Tools and Databases in Drug Discovery. In: Rudrapal, M. and Khan, J., Eds., *CADD and Informatics in Drug Discovery*, Springer, 53-77. https://doi.org/10.1007/978-981-99-1316-9_3

Supplementary Data

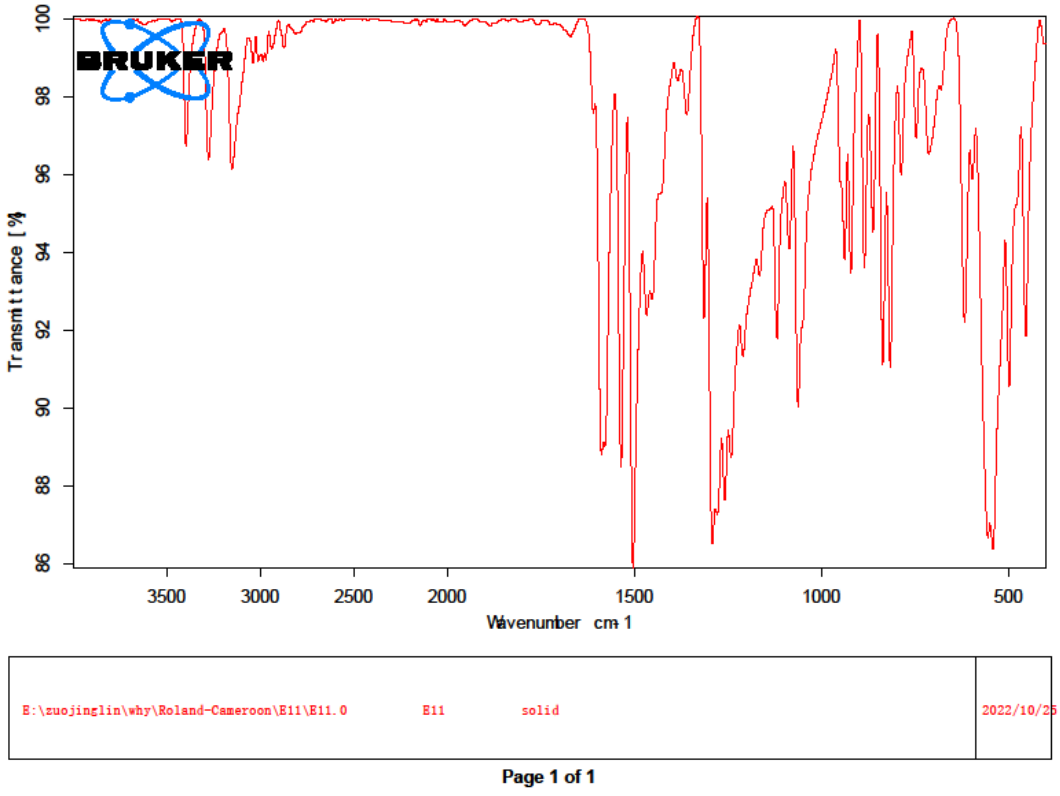

Figure S1. FT-IR spectrum of B1.

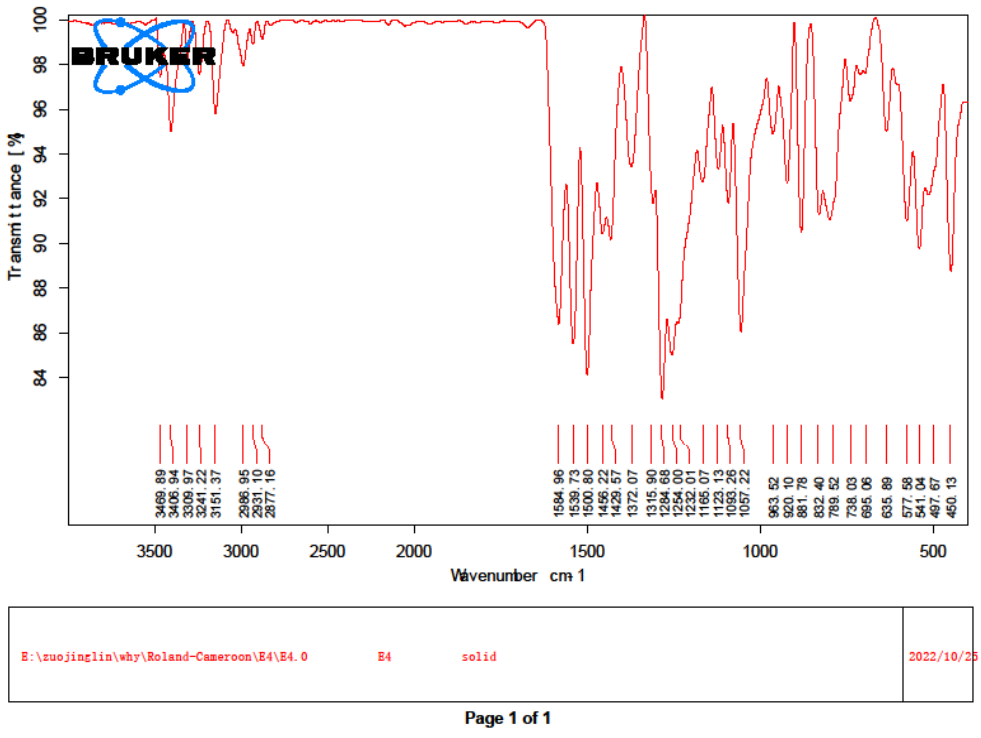

Figure S2. FT-IR spectrum of MnB1.

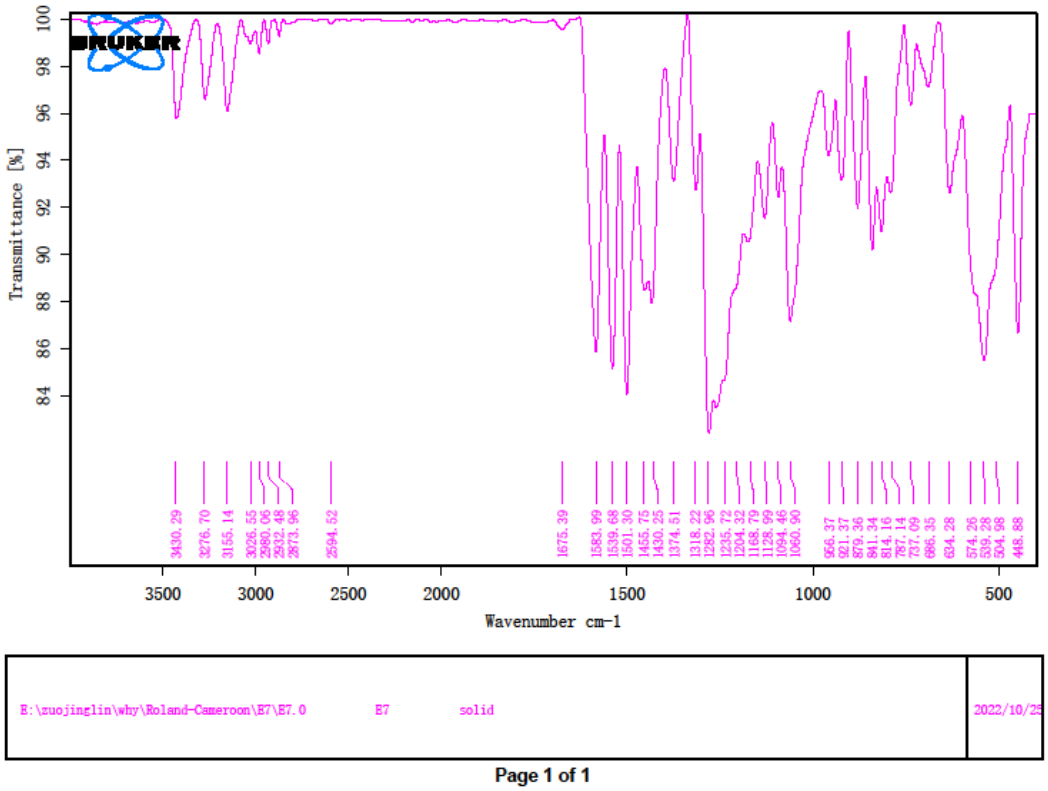

Figure S3. FT-IR spectrum of NiB1.

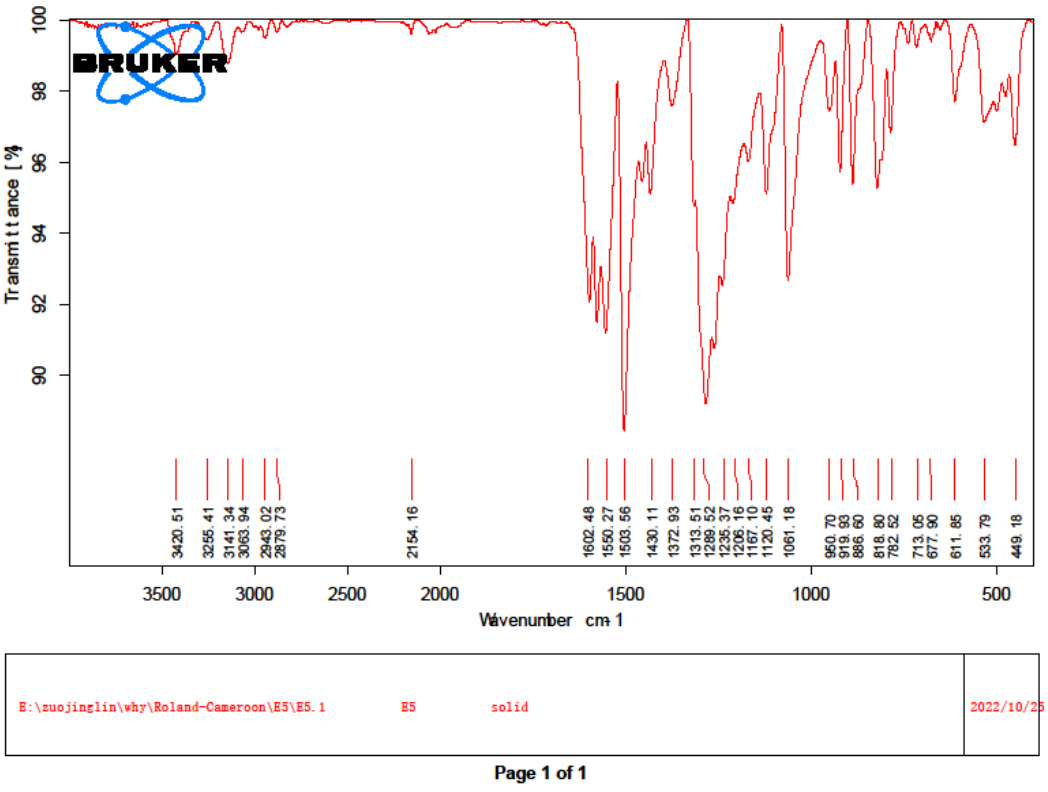

Figure S4. FT-IR spectrum of CuB1.

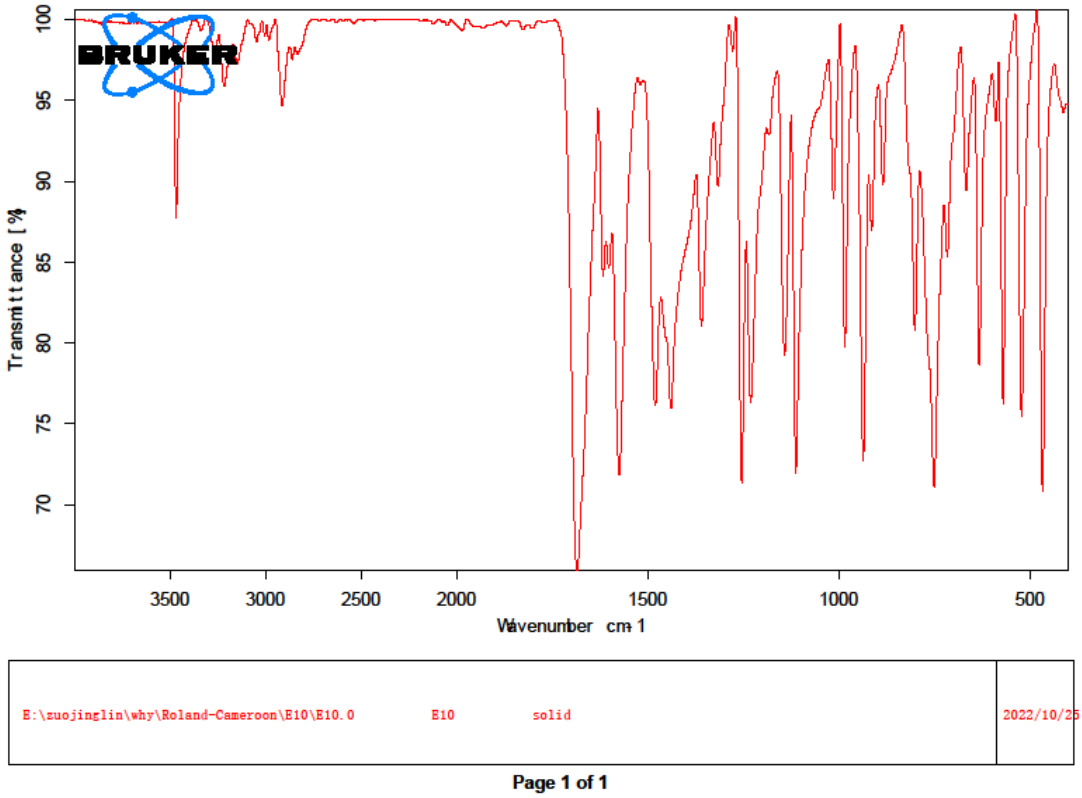

Figure S5. FT-IR spectrum of ZnB1.

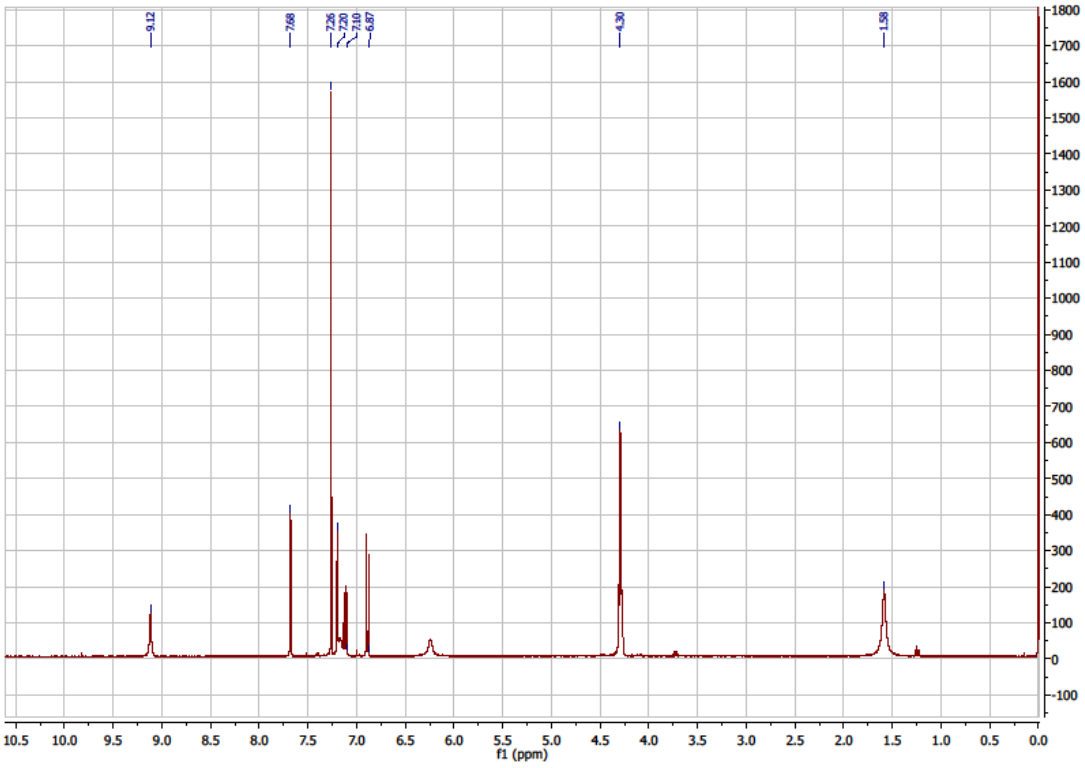

Figure S6. ^{1}H-NMR spectrum of B1.

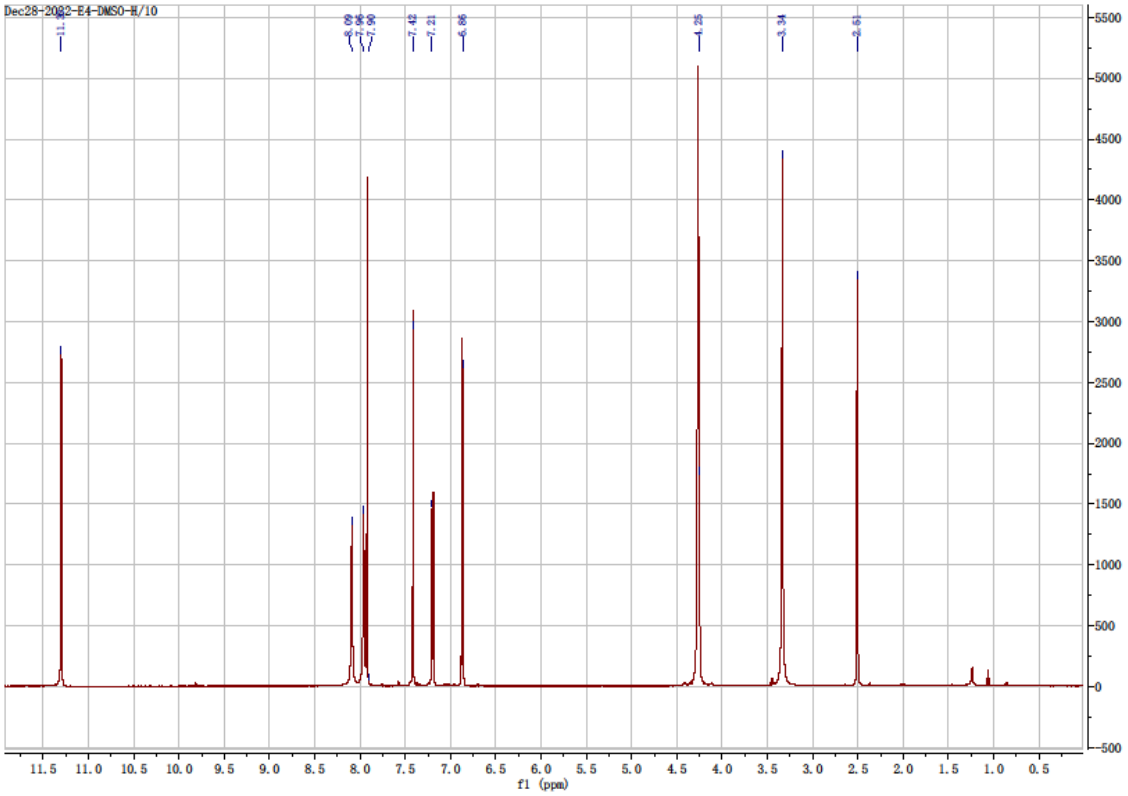

Figure S7. ^{1}H-NMR spectrum of MnB1.

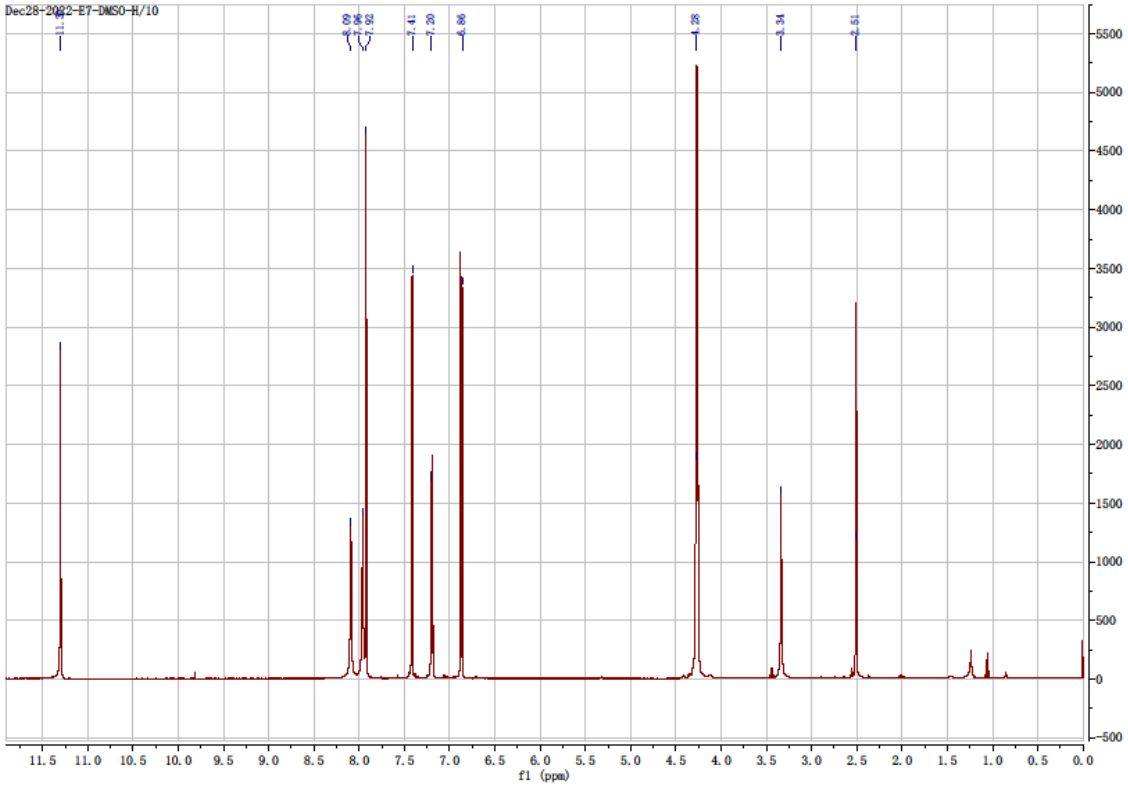

Figure S8. ^{1}H-NMR spectrum of NiB1.

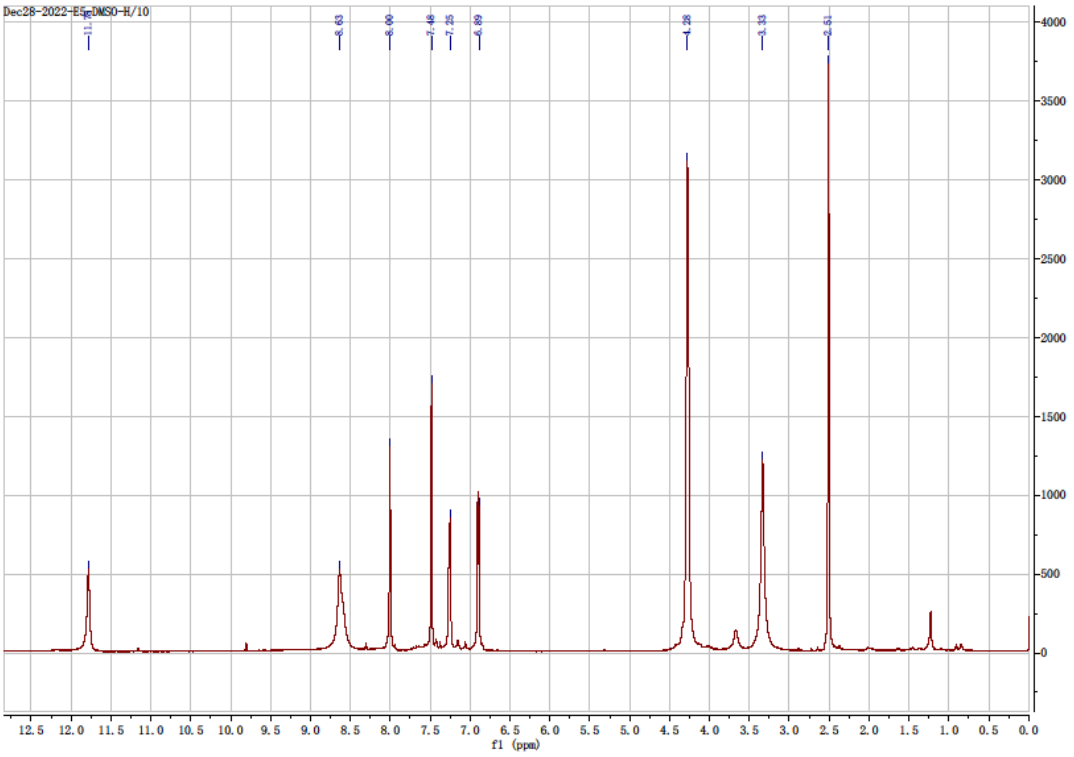

Figure S9. ^{1}H-NMR spectrum of MnB1.

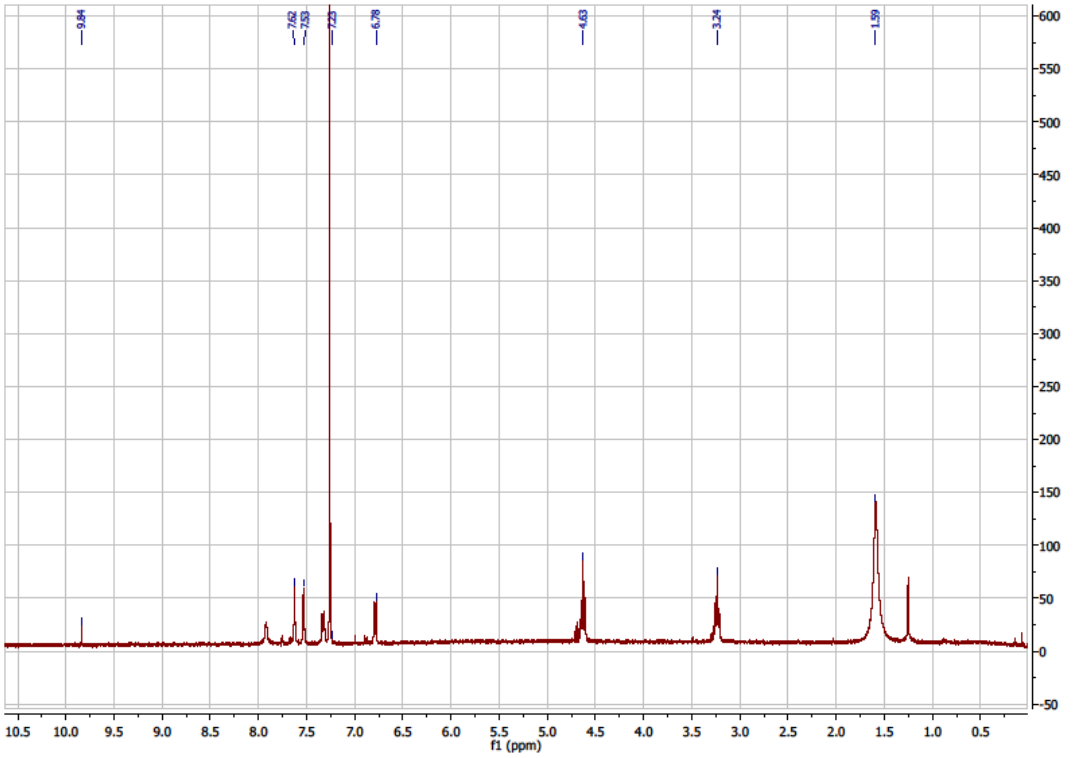

Figure S10. ^{1}H-NMR spectrum of ZnB1.